R. & M. No. 3625

R. & M. No. 3625

MINISTRY OF TECHNOLOGY

AERONAUTICAL RESEARCH COUNCIL
REPORTS AND MEMORANDA

Free-Flight Measurements of Pressure and Heat Transfer on the Lee Surface of a Delta Wing at Incidence (M = 1·0 to 3·6)

By G. H. GREENWOOD

Aerodynamics Dept., R.A.E., Farnborough

LONDON: HER MAJESTY'S STATIONERY OFFICE
1970
PRICE £1 3*s* 0*d* [£1·15] NET

Free-Flight Measurements of Pressure and Heat Transfer on the Lee Surface of a Delta Wing at Incidence (M = 1·0 to 3·6)

By G. H. GREENWOOD

Aerodynamics Dept., R.A.E., Farnborough

Reports and Memoranda No. 3625*

October, 1968

Summary.

Pressure and heat-transfer measurements have been made on the lee surface of a delta wing at 14 degrees incidence in free flight over a Mach number range of 1·0 to 3·6 and at free-stream Reynolds numbers between 6 and 24 millions based on centreline chord. A comparison is made with the results from a previous free-flight model test to assess the effect on the lee surface pressure and heat transfer of a change in sweepback angle from 65·9 to 76 degrees.

LIST OF CONTENTS

*Replaces R.A.E. Tech. Report No. 68246—A.R.C. 31 081.

LIST OF ILLUSTRATIONS

---

1. *Introduction.*

The presence of two coiled vortex sheets over the lee surface of a delta wing at incidence arising from flow separations at or near the leading edges represents a stable and controllable type of flow well-suited for practical aircraft applications. Such a flow has been observed and studied in many experiments both in the R.A.E. and elsewhere, typically those of Ref. 1 to 8, but most of the published measurements have been of pressure distributions and aerodynamic forces. Measurements of heat transfer in this type of separated flow are few, probably the most comprehensive being the FFA wind-tunnel tests of Ref. 8 made at $M_\infty = 3{\cdot}0$ for various angles of sweepback and incidence and the R.A.E. free-flight tests of Ref. 4 made at M_∞ between 2·0 and 3·6 for a sweepback angle of 76 degrees and incidence of 14 degrees.

The latest R.A.E. free-flight measurements on a delta wing at incidence are presented in this Report. These measurements consist of pressure and heat-transfer distributions made on the lee surface of a wing at the same 14 degrees incidence as the tests of Ref. 4 but for a sweepback of 65·9 degrees compared with 76 degrees for the wing of Ref. 4.

By combining the present measurements with those from Ref. 4, an assessment is made in the present Report of the effect of a change in sweepback from 76 to 65·9 degrees on the lee surface pressures and heat-transfer.

No detailed analysis of the wing flow has been attempted; the presentation is limited to graphical comparisons of the measured pressures and heat-transfer rates obtained for the two sweepback angles and to a comparison of the heat-transfer measurements with theoretical[11,12] flat-plate values. Only a very limited comparison is possible between the free-flight measurements and those from wind-tunnel tests because of incompatibilities in Mach number, incidence and wing geometry.

The results from the present tests (65·9 degrees swept wing) were obtained using two identical free-flight models, referred to in the text as Models 1 and 2, over a Mach number range of 1·0 to 3·6 at free-stream Reynolds numbers of 6 to 24 millions based on the wing centreline chord.

Because the inch was the basic unit used in the model manufacture the dimensions shown in Figs. 1 and 3 are expressed in this unit—elsewhere S.I. units have been used either solely or in support of conventional British units.

The present tests were completed in July 1967.

---

2. *Description of the Models.*

One of the operational restrictions in the use of rocket-launched free-flight models is that they should remain at all times within prescribed safety boundaries. This means that the flight path must be predictable, sometimes to a high degree of certainty—a condition best achieved by designing for a ballistic (non-lifting) trajectory.

In the present free-flight investigation it was desired to test a wing at a constant and moderately high incidence. It was necessary therefore, in order to satisfy the requirement of a ballistic trajectory, to cancel the lift of this wing by introducing into the test head another wing, a mirror image of the first, having an identical but opposing lift. The symmetrical, two-winged test head so produced is illustrated in Figs. 1 and 2.

The wing itself was a sharp-edged delta of triangular cross-section with a 65·9 degrees sweepback and an aspect ratio of 1·79. It was tested at a constant incidence of 14 degrees measured relative to the plane of its flat lee surface.

One of the mirror image pair of wings was instrumented entirely for pressure measurements and was made of steel: the other was used primarily for heat-transfer measurements, and its lee surface and a portion of the leading edge was made in the form of a thin-walled calorimeter 0·04 inch (1·0 mm) thick using electro-deposited nickel. This latter wing has 0·004 inch (0·10 mm) diameter chromel/alumel thermocouples welded to its inner surface to sense the in-flight temperature history at 24 stations on the flat lee surface and at two stations on the windward surface. These temperature measurements formed the basic experimental data from which the determinations of heat transfer were made.

Spanwise pressure measurements were also made on the nickel wing to provide a basis for computing reference heat fluxes (*see* Section 5.3.2). The locations of the pressure orifices and thermocouples for both wings are shown in Fig. 3.

Aft of the two-winged test head was a light-alloy conical fairing terminating in a cylindrical instrumentation bay which housed the radio-telemetry and radio-Doppler equipment and carried on its outer surface the transmitting and receiving aerials appropriate to these two systems. Another fairing, containing ballast for centre of gravity location, linked the instrumentation bay to a 17 inches (432 mm) diameter solid-fuel rocket motor. The complete assembly, illustrated in Fig. 2, was aerodynamically stabilized by a 3-panel fin unit attached just forward of the rocket-motor nozzle.

In-flight incidence of the test head in pitch was continuously monitored by measurements of the pressure differential between the windward surfaces of the two wings and in yaw by measurements of the differential pressure between the two facets of the angled windward surface of the steel wing (Fig. 1). The necessary incidence/pressure calibrations were obtained from wind-tunnel tests using a scaled model of the test head.

Two linear accelerometers were used to monitor accelerations normal to the axis of the test vehicle to provide an additional measure of flight incidence.

Two identical test vehicles of the above description were used; these are subsequently referred to as Models 1 and 2. Model 1 provided data up to $M_\infty = 2{\cdot}8$ only and Model 2 was used to extend the measurements to $M_\infty = 3{\cdot}6$.

3. *Method of Test.*

The test procedures used were standard applications of the rocket-boosted free-flight model technique described in Refs. 9 and 10.

Briefly, each model was boosted into free flight at the Aberporth weapons range using a solid-fuel rocket motor to which the test head remained rigidly attached at all times. In-flight signals from the pressure transducers, accelerometers and thermocouples were sampled in a pre-determined sequence by a time-multiplexing switch and then telemetered to a ground recording-station in the form of frequency modulations of the 465 MHz subcarrier telemetry frequency. The recorded data were converted automatically from analogue to digital form and subsequently reduced to variations of pressure, acceleration, wall temperature and heat transfer with free-stream Mach number on a high-speed computer (Mercury).

Trajectory data, i.e. velocity and space co-ordinates for each model, were obtained from multiple

kinetheodolite observations made from the range shore stations and also from combined kinetheodolites and radio-Doppler trackings. Atmospheric ambient pressure and temperature at the flight altitudes were obtained from radiosonde measurements made about the time of each test.

4. *Test Conditions.*

The test conditions for both models are summarised in Fig. 4 as variations of altitude, velocity, Mach number, ambient static pressure and Reynolds number with flight time.

5. *Results and Discussion.*

The sweepback angle of the wing was 65·9 degrees and of particular interest were any differences in the surface-pressure and heat-transfer data arising from whether the Mach number normal to the leading edge, M_N, was subsonic or supersonic. M_N for a wing at incidence $\alpha°$ and having a sweepback $\Lambda°$ may be obtained from the relationship:

$$M_N = M_\infty \cos \Lambda (1 + \sin^2 \alpha \tan^2 \Lambda)^{\frac{1}{2}}$$

where M_∞ is the free-stream Mach number. For the present wing $M_N = 1{\cdot}0$ (i.e. the leading edges are nominally sonic) when $M_\infty = 2{\cdot}16$*.

Another factor likely to influence the flow is whether the leading-edge shock at M_N was attached or detached. For the present wing the leading-edge angle (measured normal to the leading edge) was 27·3 degrees and shock attachment would not therefore be expected below $M_N = 2{\cdot}25$ corresponding to a free-stream Mach number $M_\infty = 4{\cdot}83$. Since the maximum free-stream Mach number of the present tests was only 3·61 it follows that at no time was the leading-edge shock attached.

From the above the leading edges can be described as having a detached shock at all free-stream Mach numbers, subsonic normal Mach numbers (M_N) at free-stream speeds below $M_\infty = 2{\cdot}16$ and supersonic normal Mach numbers above this speed.

It will be seen from the presented experimental data that there were no measurable effects on the pressure and heat transfer resulting from a change from subsonic to supersonic values of the normal Mach number M_N.

5.1. *Flight Incidence.*

Values of flight incidence obtained from the pressure and normal accelerometer measurements are presented in Fig. 5 for both models.

The values obtained from the accelerometer data are subject to rather more uncertainty than those from the pressure measurements because the latter are related directly to incidence through the wind-tunnel calibrations (*see* Section 2) whereas the data from the accelerometers must, in the present case, be combined with assumed values of the overall vehicle lift-curve slope to yield incidence. Consequently the insidence obtained from the pressure source is considered the more reliable and, from Fig. 5, a pitch incidence of about one degree positive is accepted for Model 1 and about one degree negative for Model 2. The sign convention is that of Fig. 5.

Incidence in yaw for model 1 is judged from Fig. 5 to be indeterminate but probably less than one degree and for Model 2 to be negligibly small.

5.2. *Pressure Measurements.*

All the pressure measurements, with the exception of those used for monitoring incidence, have been presented in terms of the free-stream ambient static pressure, p_∞, as the ratio p/p_∞. These measurements

*Neglecting incidence, the value of M_∞ for $M_N = 1{\cdot}0$ is;

$$M_N \sec \Lambda = \sec 65{\cdot}9° = 2{\cdot}45 .$$

have been presented only for the accelerating phase of the flight to correspond with the heat-transfer measurements (*see* Section 5.3 below).

5.2.1. *Chordwise pressure distributions; evidence of conical flow.* The measured pressure distributions along the wing centreline chord and along a ray from the wing apex at 0·6 of the local semi-span, seen in Fig. 6, indicate that the surface flow was generally conical in nature on both models.

There are, however, some departures from a constant chordwise pressure at particular stations and free-stream Mach numbers—this is particularly so for the distribution along the centreline chord ($y/s = 1{\cdot}0$)* of both models at $M_\infty = 1{\cdot}5$ where a pronounced pressure gradient, increasing towards the base of the wing, was measured. This is believed (in the absence of any other plausible explanation) to be caused by interference from the conical support fairing and is seen to disappear at high Mach numbers except for a small residual effect confined to the last centreline chord orifice on Model 1.

Another feature of the chordwise pressure distributions is the sharp drop in pressure indicated by the broken lines of Fig. 6b for Model 2 at $x/c = 0{\cdot}75$ for the spanwise station $y/s = 0{\cdot}6$. Such a pressure drop was not measured at this station on Model 1 and this would suggest the possibility of a spurious response from the particular pressure transducer concerned. This particular orifice was coded P23 in the model design schedule and for completeness the responses from orifices P21 and P25 on each side of P23 on the same conical generator are shown in Fig. 7 together with the response from P23 over the relevant Mach number range during *decelerating* flight. This latter presentation shows that the pressure drop is in fact present during decelerating flight but occurs at a slightly lower Mach number; the responses from the adjacent orifices P21 and P25 do not, however, show a pressure drop and no explanation can be offered for this apparently anomolous pressure variation at orifice P23.

5.2.2. *Spanwise pressure distributions; evidence of vortical flow.* The spanwise pressure distributions for both models are shown in Figs. 8 and 9; the heat-transfer data in these figures will be discussed in Section 5.3.2 and the data relevant to Ref. 4 will be discussed in Section 5.4.

The pressure distributions of Fig. 8 are in fact identical to those of Fig. 9 and represent measurements from the spanwise orifice array at $x/c = 0{\cdot}975$ on the heat-transfer (nickel) wing of Models 1 and 2. The use of these pressures, obtained at the longitudinal station $x/c = 0{\cdot}975$, for comparison with heating data obtained at $x/c = 0{\cdot}75$ and 0·875 in Figs. 8 and 9 is justified by the generally conical nature of the flow seen in Fig. 6 although strictly some departures from conical flow are apparent at the $x/c = 0{\cdot}975$ station in Fig. 6.

It is evident from the variation of p/p_∞ with spanwise position that the flow over the suction surface of the wing was consistent with the well-known vortex type in which the flow separates at or near the leading edge and reattaches to the surface at some distance inboard. In this type of flow some of the reattached air separates again between the inboard reattachment region and the leading edge to form a coiled vortex above the wing surface. This flow regime results in a characteristic spanwise pressure distribution with high pressures in the inboard reattachment region falling rapidly in the cross-flow region to a minimum prior to the secondary separation and rising again towards the leading edge.

The influence of Mach number on the spanwise pressure distribution is clearly revealed in Fig. 8. At the lower Mach numbers the characteristic spanwise pressure gradient is very pronounced, but at higher Mach numbers the gradient becomes increasingly smaller as indeed does the general level of the pressure over the whole wing surface.

A notable feature of the manner in which the surface pressure varies with the free-stream Mach number is the peak that occurs between $M_\infty = 1{\cdot}0$ and 1·5. This is best seen in Fig. 10 which shows the variation with Mach number of the surface pressure at each of the ten spanwise orifices located at the chordwise station $x/c = 0{\cdot}975$. At spanwise stations $y/s = 1{\cdot}0$ to 0·8 the surface pressure is seen to reach a peak at

*The ratio $y/s = 1{\cdot}0$ refers to the spanwise station at the wing centreline and $y/s = 0$ to the leading edge—this is the reverse of conventional notation and was adopted for consistency with the presentation of Ref. 4 which in turn followed the presentation of Thomann in Ref. 8.

about $M_\infty = 1{\cdot}5$ but at the outboard spanwise stations $y/s = 0{\cdot}7$ to $0{\cdot}1$ the pressure peak occurs at a somewhat lower Mach number.

It is noted that there is no evidence from the present test of a similar peak in the heat-transfer measurements in this Mach number region (*see* Fig. 14).

5.3. *Heat-Transfer Measurements.*

Only heat-transfer data obtained during the accelerating (heating) phase of the test have been presented. This is because the determinations of heat flux becomes less accurate as zero-heat-transfer conditions are approached.

5.3.1. *Heat flux and wall temperature.* The experimental net local heat flux, q, from the boundary layer to the model surface was obtained from the thermocouple measurements of the temperature of the inside surface of the wall, T_w, using the analysis described in Ref. 10.

Typical variations of q and T_w with flight time and Mach number for three stations on Model 2 are presented in Fig. 11 where it is seen that the maximum values of q and T_w for stations on the lee surface are considerably less than those for a station on the windward surface.

In Fig. 12 typical spanwise distributions of q and T_w on the lee surface of Models 1 and 2 are presented for two Mach numbers. Since the magnitude of q and T_w is dependent upon the particular thickness and thermal properties of the wall Fig. 12 serves mainly to illustrate the consistency between models of the primary data and in particular the wall temperature measurements.

5.3.2. *Heat-transfer factors, h.* The heat-transfer factor, h, used in the presentation is defined at

$$h = \frac{q}{T_r - T_w}$$

where T_w is the measured wall temperature and T_r the recovery temperature calculated using an assumed turbulent recovery factor of $0{\cdot}89$[11].

In keeping with Ref. 4 the heat-transfer factor, h, is presented in terms of two theoretical factors h_{LOC} and h_∞ as h/h_{LOC} and h/h_∞, where

h_{LOC} is the theoretical heat-transfer factor calculated from Eckert's intermediate enthalpy theory[11,12] appropriate to a flat plate at the measured local wall temperature with a fully turbulent boundary layer having flow conditions evaluated on the basis of an isentropic expansion from free-stream pressure to the measured local surface pressure. The reference length was taken as the wetted distance of the particular station from the wing leading edge in the free-stream direction,

h_∞ is identical to h_{LOC} except that free-stream ambient static pressures were used instead of the measured local surface pressures.

The skin-friction law used in these calculations was

$$C_f = 0{\cdot}288\,(\log_{10} Re_x^*)^{-2{\cdot}45} \qquad \text{equation (12) Ref. 11}$$

and a Reynolds analogy factor

$$\frac{St}{\frac{1}{2}C_f} = 1.22 \qquad \text{Ref. 11}$$

was assumed. The asterisk (*) indicates that the air properties were evaluated at intermediate enthalpy(i^*) conditions defined by

$$i^* = i_e + 0{\cdot}5\,(i_w - i_e) + 0{\cdot}22\,(i_r - i_e) \qquad \text{equation (3), Ref. 11}$$

for which an enthalpy recovery factor of 0·89[11] was assumed. Suffix e refers to conditions at the edge of the boundary layer, suffix r to recovery conditions and w to the wall.

Because h_{LOC} is based on measured local pressures it is more likely to collapse the experimental heat-transfer data completely than is h_∞ – the values of h/h_{LOC} should be unity for stations in a boundary layer turbulent from the wing leading edge.

On the other hand the ratio h/h_∞ allows an immediate appreciation of the relative magnitude of the measured heat transfer to that appropriate to a flat plate at zero incidence in the free-stream. Its use as a reference heat flux may be considered analogous to the use of the free-stream pressure (p_∞) to correlate surface pressure measurements.

5.3.3. *Chordwise heat-transfer distributions.* The variation of heat transfer along the wing centreline chord for a range of Mach numbers is presented in Fig. 13 together with some pressure distributions for comparison.

Most notable in this presentation are the differences in the heat-transfer ratios h/h_{LOC} and h/h_∞ between Models 1 and 2 particularly at the chordwise stations $x/c = 0{\cdot}375$ and 0·5. On Model 1 the heat-transfer ratios at these forward chordwise stations are generally lower than those on the stations near the base of the wing, i.e. at stations $x/c = 0{\cdot}75$ and 0·875.

These comparatively low heating rates towards the wing apex are consistent with the boundary layer at the forward stations being either laminar or transitional in character. This is not supported, however, by the results from Model 2 which for a nominally identical wing show generally higher values of the heat-transfer ratios at the forward stations compared with those from Model 1; these higher values on Model 2 are more consistent with a fully turbulent boundary layer which may have existed on Model 2, and not on Model 1, as the result of small physical differences.

The effect of Mach number on the ratio h/h_{LOC} is particularly evident for Model 2 at the chordwise stations $x/c \leqslant 0{\cdot}75$ in Fig. 13. At these stations the heat-transfer ratio is seen to show increasingly larger discrepancies from the predicted value $h/h_{LOC} = 1{\cdot}0$ as the Mach number increases; part of this discrepancy may be due to the reduced accuracy in computing h_{LOC} due to the much lower surface pressures at the higher Mach numbers.

5.3.4. *Spanwise heat-transfer distributions.* The spanwise distributions of the heat-transfer ratios h/h_{LOC} and h/h_∞ at the chordwise positions $x/c = 0{\cdot}875$ and 0·75 are presented in Figs. 8 and 9 respectively.

The results from Ref. 4, included in Figs. 8 and 9, will be the subject of discussion in Section 5.4.

It will be seen in Figs. 8 and 9 that the heat-transfer data lie generally in the region $h/h_{LOC} = 1{\cdot}0$ and, although there is some variation in magnitude between particular Mach numbers, the results demonstrate the basic efficacy of the theory of Ref. 11 in predicting turbulent boundary-layer heat flux in a known pressure field.

The spanwise variation of h/h_∞ indicates that the distribution of heat-transfer rates follows closely that of the surface pressure. Where the latter is high the heat-transfer rate is high and conversely there is a low heat-transfer rate in the regions of low pressure; the distribution of heat-transfer rate is in fact entirely consistent with the existence of a separated-vortex type of flow over the wing lee surface.

Fig. 14 shows the variation with Mach number of the heat transfer at each of the spanwise stations at the chordwise position $x/c = 0{\cdot}875$. This indicates clearly a reduction of heat transfer with increasing Mach number following a similar trend exhibited by the surface pressure seen in Fig. 10. The heat-transfer variations of Fig. 14 do not, however, exhibit a peak between $M_\infty = 1{\cdot}0$ and 1·5 as seen in Fig. 10 for the pressure variations.

5.4. *Effect of Increased Sweepback* (comparison with Model 1 of Ref. 4).

Model 1 of Ref. 4 was identical in all significant respects to the models of the present tests except that the leading-edge sweepback angle was 76 degrees compared with the present 65·9 degrees. Since the test conditions were substantially the same the results from Ref. 4 may be compared directly with those from the present tests in order to assess the effect of a change in sweepback on the surface pressure and heat transfer.

In Figs. 8 and 9 spanwise distributions of pressure and heat transfer from Ref. 4 are compared where possible with similar measurements from the present tests and in Figs. 10 and 14 similar comparisons are made for the variations with Mach number of the pressures and heat transfer at individual spanwise stations.

These comparisons reveal differences

$$\Delta\left(\frac{p}{p_\infty}\right) \text{and} \ \Delta\left(\frac{h}{h_\infty}\right)$$

defined as

$$\Delta\left(\frac{p}{p_\infty}\right) = \left(\frac{p}{p_\infty}\right)_{\Lambda=76^\circ} - \left(\frac{p}{p_\infty}\right)_{\Lambda=65{\cdot}9^\circ} \qquad \text{(from Fig. 10)}$$

and

$$\Delta\left(\frac{h}{h_r}\right) = \left(\frac{h}{h_r}\right)_{\Lambda=76^\circ} - \left(\frac{h}{h_r}\right)_{\Lambda=65{\cdot}9} \qquad \text{(from Fig. 14)}$$

where $(p/p_\infty)_{\Lambda\ =65{\cdot}9}$ and $(h/h_\infty)_{\Lambda=65{\cdot}9^\circ}$ are the mean values from Models 1 and 2 at $M_\infty < 2{\cdot}7$ and the values for Model 2 at $M_\infty > 2{\cdot}7$.

These differences are presented in Figs. 15 and 16 as fractions of the pressure and heat transfer appropriate to the 65·9 degrees swept wing—a positive sign indicating an increase in the measured quantity for a change in sweepback from 65·9 to 76 degrees.

Figs. 17 and 18 summarize most effectively the result of increasing the sweepback angle; Fig. 17 shows that the pressures have been very little affected in the region of the wing centreline chord ($y/s = 1{\cdot}0$) at all Mach numbers whereas near the leading edge ($y/s = 0$) the pressures have been generally doubled. It should be noted, however, that the pressure levels in the leading-edge region ($y/s \leqslant 0{\cdot}4$) were in fact generally very small for the 65·9 degree swept wing being typically less than 0·25 of the ambient static pressure at Mach numbers above 1·5 (*see* Fig. 10). Quantitatively, therefore, the pressure increments in the leading-edge region due to the change in sweepback were in themselves very small.

Fig. 17 also shows that for Mach numbers above 2·5 (upper figure) there has been a general diminution of pressure in the mid semi-span region ($0{\cdot}4 < y/s < 0{\cdot}8$) due to the increased sweepback. At the lower Mach numbers (lower figure, Fig. 17) the region of diminished pressure is less extensive and in this case the pressure diminution for increased sweepback is very small.

Fig. 18 shows that the effect of the change in sweepback on the heat-transfer distribution is broadly similar to that seen for the pressures in Fig. 17. Some diminution in heat transfer is apparent in the mid semi-span region for Mach numbers of 2·5 and above and an increase in heating is seen in the leading-edge region at all Mach numbers.

5.5. *Comparison with Wind-Tunnel Tests.*

In Figs. 19, 20 and 21 comparisons are made between the free-flight measurements of spanwise pressure distributions and those from the wind-tunnel tests of Refs. 8 and 13. Because of incompatibilities in Mach number, incidence and wing geometry these free-flight/wind tunnel comparisons cannot be entirely consistent; for example the comparisons in Figs. 19 and 21 are consistent only in Mach number, incidence and sweepback with large disparities in model cross-section. In Fig. 20 there is consistency only in Mach number and incidence with disparities in both sweepback and model cross-section.

These comparisons nevertheless serve to illustrate the measure of agreement obtained between the different test facilities in the distribution and variation with sweepback of the lee-surface pressure on basically similar wings; they are in fact mutually corroborative of the salient features of the pressure distributions. In this respect comparison of the free-flight pressure distributions with those of Ref. 8 in

Fig. 21 shows corroboration of the trend towards decreased surface pressures in mid-span as sweepback is increased.

The only wind-tunnel heat-transfer measurements having relevance to the free-flight tests are those of Thomann presented in Ref. 8. Thomann's measurements, at $M_\infty = 3{\cdot}0$ only, are presented in the form of Stanton number and as such are not directly comparable with the heat-transfer ratios of the free-flight tests. Thomann found, however, the same quantitative dependence of heat transfer upon the surface pressure level as was found in the free-flight tests.

6. *Conclusions.*

Measurements of surface pressures and heat-transfer rates have been made on the lee surface of a delta wing at 65·9 degrees sweepback at 14 degrees incidence in free-flight over a Mach number range of 1·0 to 3·6 and at free-stream Reynolds numbers between 6 and 24 millions based on centreline chord.

The main conclusions arising from these measurements are:

(1) The spanwise pressure distributions are consistent with the occurrence of a vortex-type flow over the lee surface and the associated spanwise pressure gradients are large for the lower free-stream Mach numbers but become smaller as Mach number is increased. This trend is accompanied by a general reduction in the pressure level over the whole lee surface of the wing.

(2) The chordwise pressure distributions show that the flow over the lee surface is generally conical in character.

(3) The magnitude and distribution of aerodynamic heat-transfer rates to the wing surface follow very closely the magnitude and distribution of the local surface pressures.

(4) The use of a theoretical heat-transfer factor, h_{LOC}, based on Eckert's[11,12] intermediate-enthalpy theory and using local flow conditions derived in turn from the measured local surface pressures, is shown to predict the heat-transfer data more successfully than the use of a similar theoretical factor, h_∞, based on the same theory but using flow conditions appropriate to the free stream.

(5) No discernible discontinuities are present in the variation with Mach number of the heat-transfer rates or surface pressures to suggest that the flow over the wing was significantly different for subsonic as opposed to nominally supersonic leading edges.

(6) Comparison of the present results, appropriate to a sweepback angle of 65·9 degrees and incidence of 14 degrees, with the results from Ref. 4 for a wing of 76 degrees sweepback at the same incidence, shows consistently higher pressures for the 76 degrees swept wing in the region of the leading edge at all Mach numbers but only small changes are seen near the wing centreline chord. The pressures in the mid semi-span region are markedly lower for the 76 degrees swept wing at $M_\infty = 2{\cdot}5$ and above. Corroboration for these trends is found in the wind-tunnel tests of Ref. 8 (*see* Fig. 21 of present Report).

(7) The effect of the change in sweepback on the heat transfer was broadly the same as the effect on the pressures—a higher heating rate in the region of the leading edges for the 76 degrees swept wing at all Mach numbers and a diminution of heating for this wing in the mid semi-span region at $M_\infty = 2{\cdot}5$ and above. In the region of the centreline chord only small effects arising from the change of sweepback were found.

LIST OF SYMBOLS

c	Centreline chord
C_f	Skin-friction coefficient
h	Heat-transfer factor $= q/T_r - T_w$
m	Metres
M	Mach number
N	Newton, unit of force (unit of pressure when used as N/m^2)
p	Static pressure
q	Aerodynamic heat flux
Re	Reynolds number
s	Local semi-span
St	Stanton number
T	Temperature °K
x	Chordwise co-ordinate measured aft from wing apex in the plane of the flat lee surface of the wing
y	Spanwise co-ordinate measured from local leading edge
α	Pitch incidence
β	Yaw incidence
Δ	An increment
Λ	Angle of leading-edge sweepback

Suffices

e	Referred to conditions at the edge of the boundary layer
LOC	Referred to local conditions
N	Normal to leading edge
r	Recovery conditions
w	Wall conditions
∞	Referred to free-stream conditions

REFERENCES

No.	*Author(s)*	*Title, etc.*
1	J. W. Britton	Pressure measurements at supersonic speeds on three uncambered conical wings of unit aspect ratio. A.R.C. C.P. 641 (1962).

REFERENCES—*continued*

No.	*Author(s)*	*Title, etc.*
2	L. A. Wyatt and L. F. East ..	Low speed measurements of skin-friction on a large half-model slender wing. A.R.C. C.P. 1107.
3	A. Stanbrook and L. C. Squire	Possible types of flow at swept leading edges. R.A.E. Technical Note Aero 2608 (A.R.C. 21464) (1959).
4	J. B. W. Edwards	Heat-transfer and pressure measurements on the upper surface of a delta wing at incidence at Mach numbers between 2·0 and 3·6. A.R.C. R. & M. 3469 (1965).
5	L. C. Squire	Pressure distributions and flow patterns at $M = 4{\cdot}0$ on some delta wings. A.R.C. R. & M. 3373 (1963).
6	L. C. Squire, J. G. Jones and A. Stanbrook ..	An experimental investigation of the characteristics of some plane and cambered 65° delta wings at Mach numbers from 0·7 to 2·0. A.R.C. R. & M. 3305 (1961).
7	L. C. Squire	Pressure distributions and flow patterns on some conical shapes with sharp edges and symmetrical cross-sections at $M = 4{\cdot}0$. A.R.C. R. & M. 3340 (1962).
8	H. Thomann	Measurements of heat transfer, recovery temperature and pressure distributions on delta wings at $M = 3{\cdot}0$. Sweden, FFA Report 93 (1963).
9	J. A. Hamilton and P. A. Hufton	Free flight techniques for high speed aerodynamic research. Jl. R. aeronaut. Soc., pp 151–177 (1956).
10	J. Picken and D. Walker ..	Techniques for the investigation of aerodynamic-heating effects in free flight. AGARD Report 376 (1961). R.A.E. Technical Note Aero 2758 (A.R.C. 23125) (1961).
11	L. F. Crabtree, R. L. Dommett, and J. G. Woodley	Estimation of heat transfer to flat plates, cones and blunt bodies. R.A.E. Technical Report 65137 (A.R.C. 27233) (1965).
12	R. J. Monaghan	Formulae and approximations for aerodynamic heating rates in high speed flight. A.R.C. C.P. 360 (1955)
13	J. A. Rein	Flow over the suction surface of sharp edge delta wings with detached leading edge shock waves. W.R.E. Technical Note HSA 102 (1964).

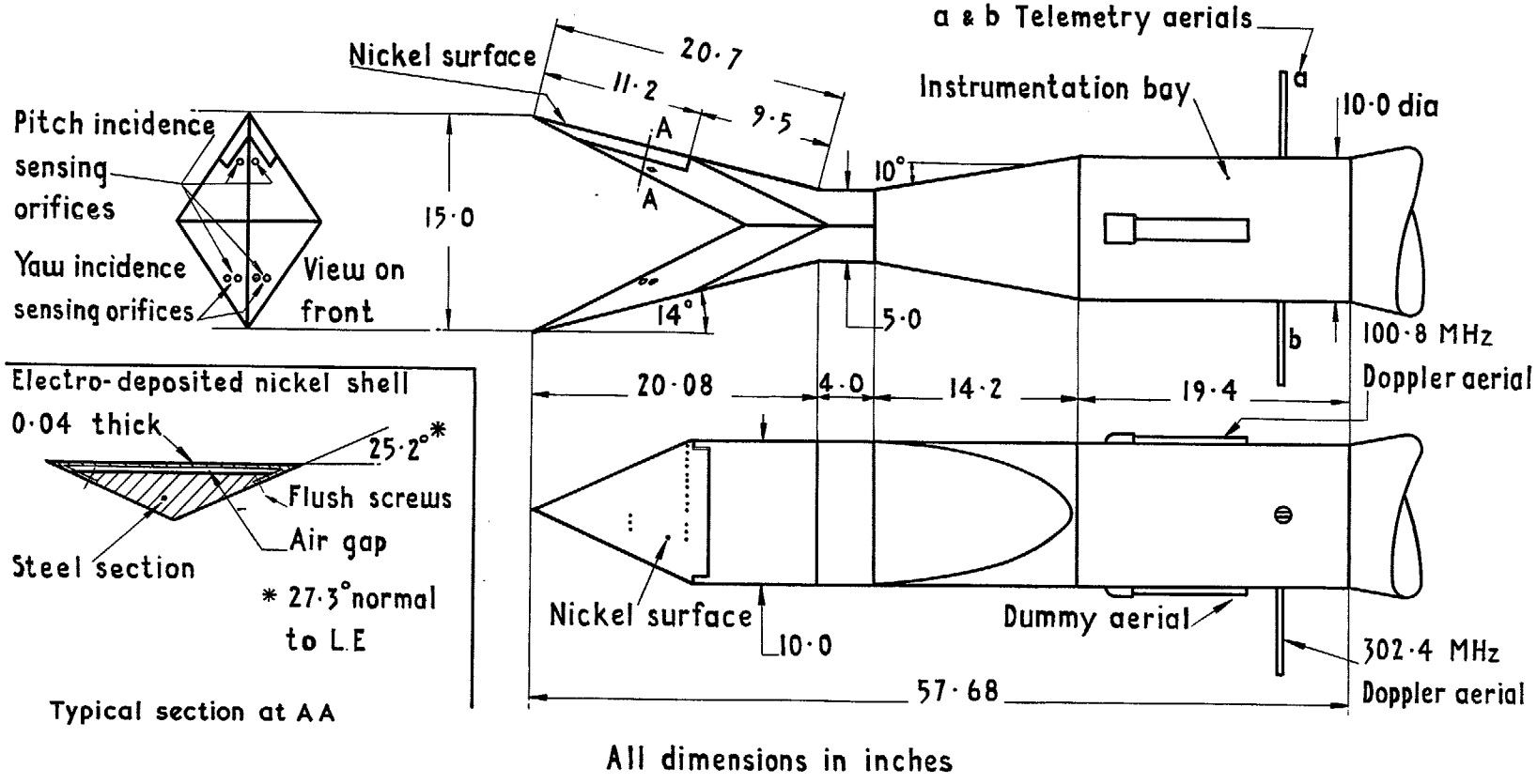

FIG. 1. General arrangement of test head (Models 1 & 2).

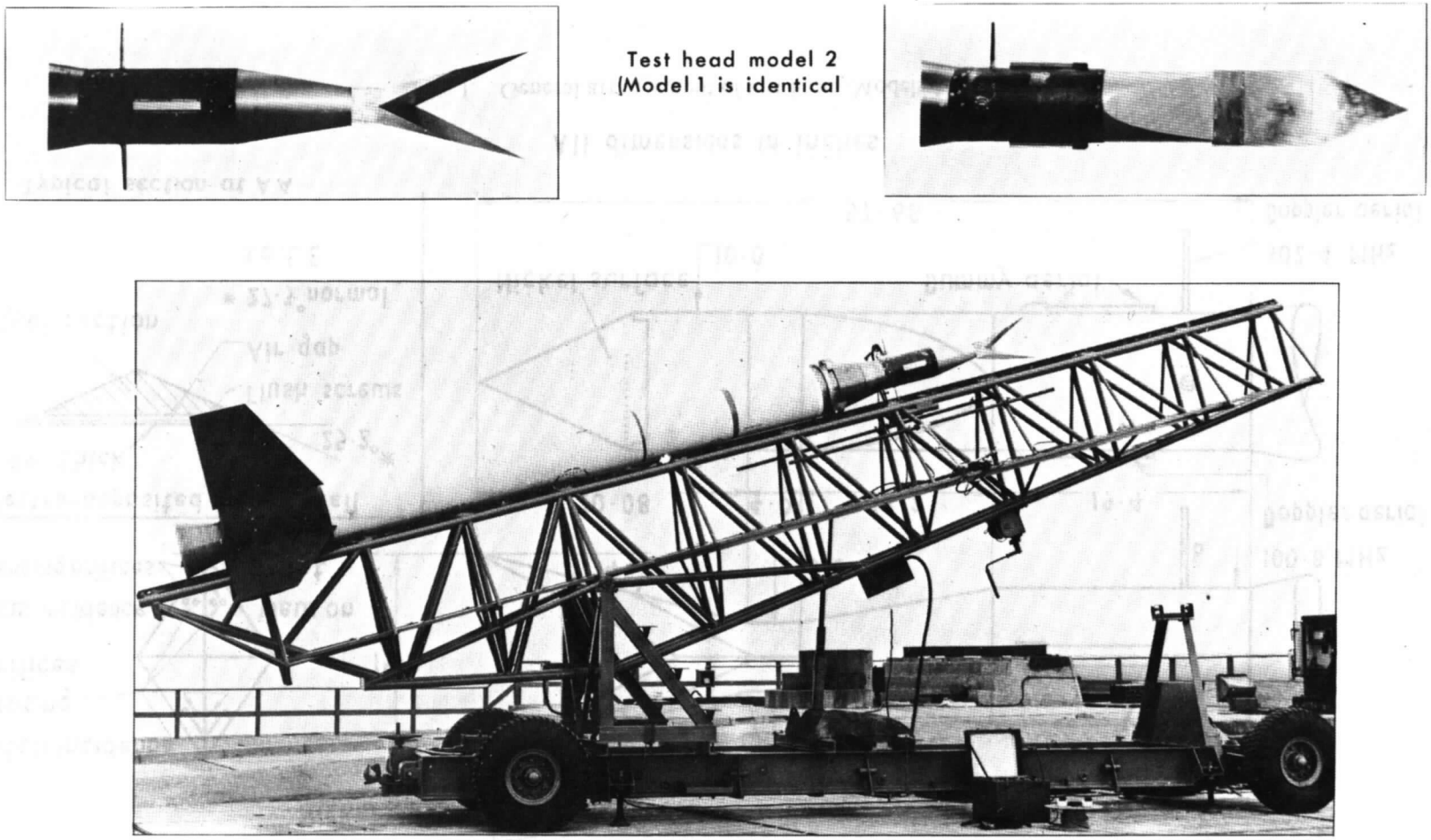

FIG. 2. Complete assembly on launcher and test head (Model 2).

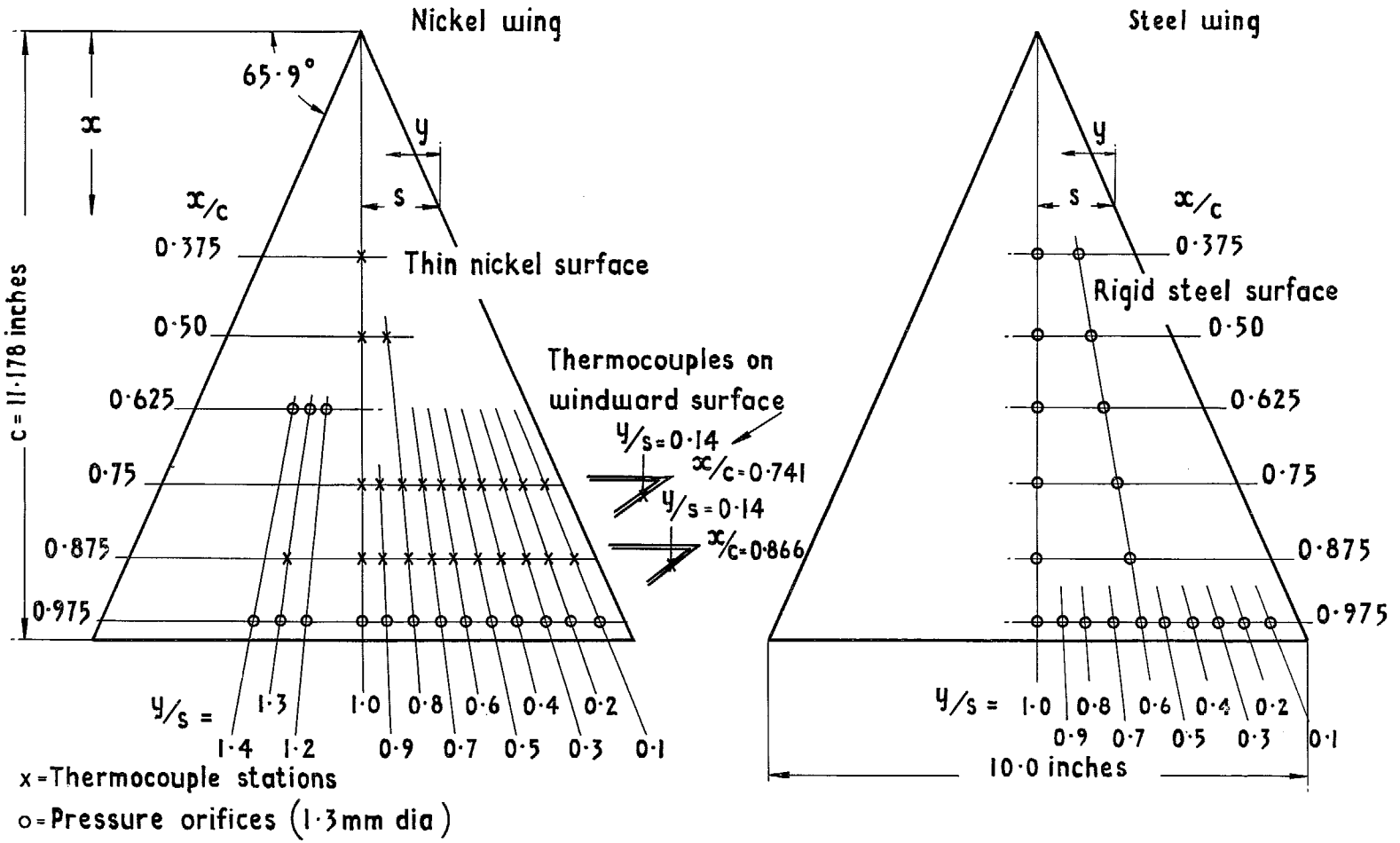

FIG. 3. Thermocouple and pressure orifice stations (Models 1 & 2).

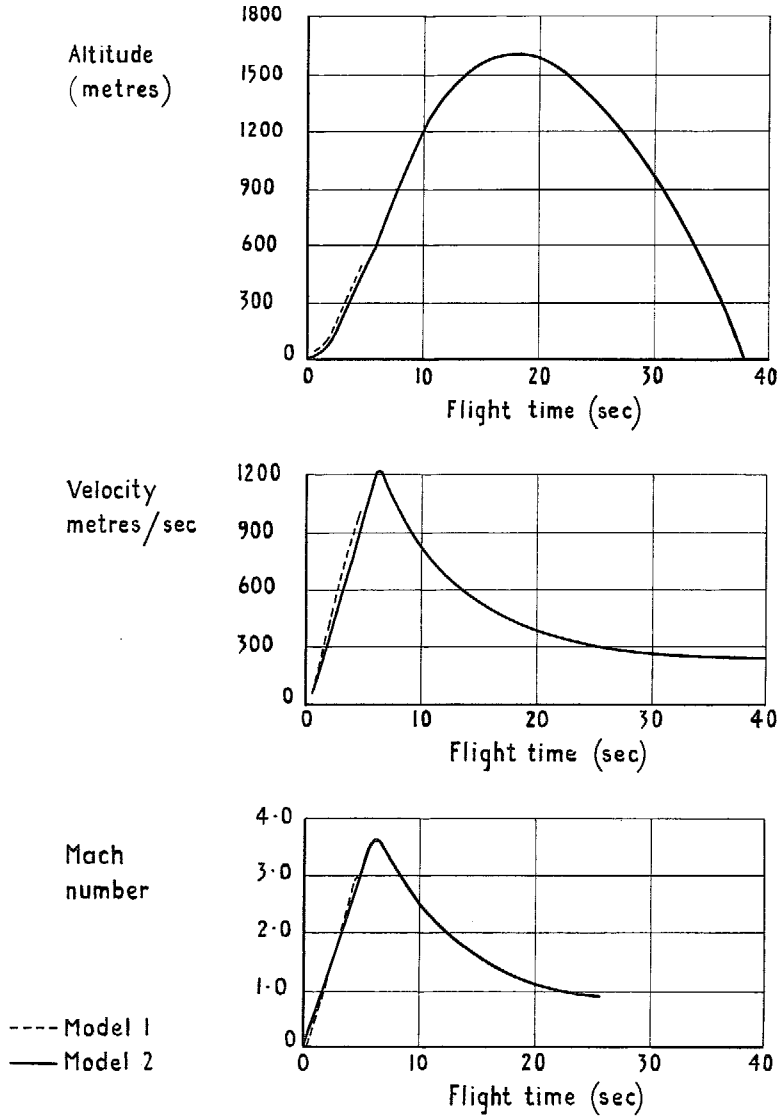

FIG. 4. Test conditions.

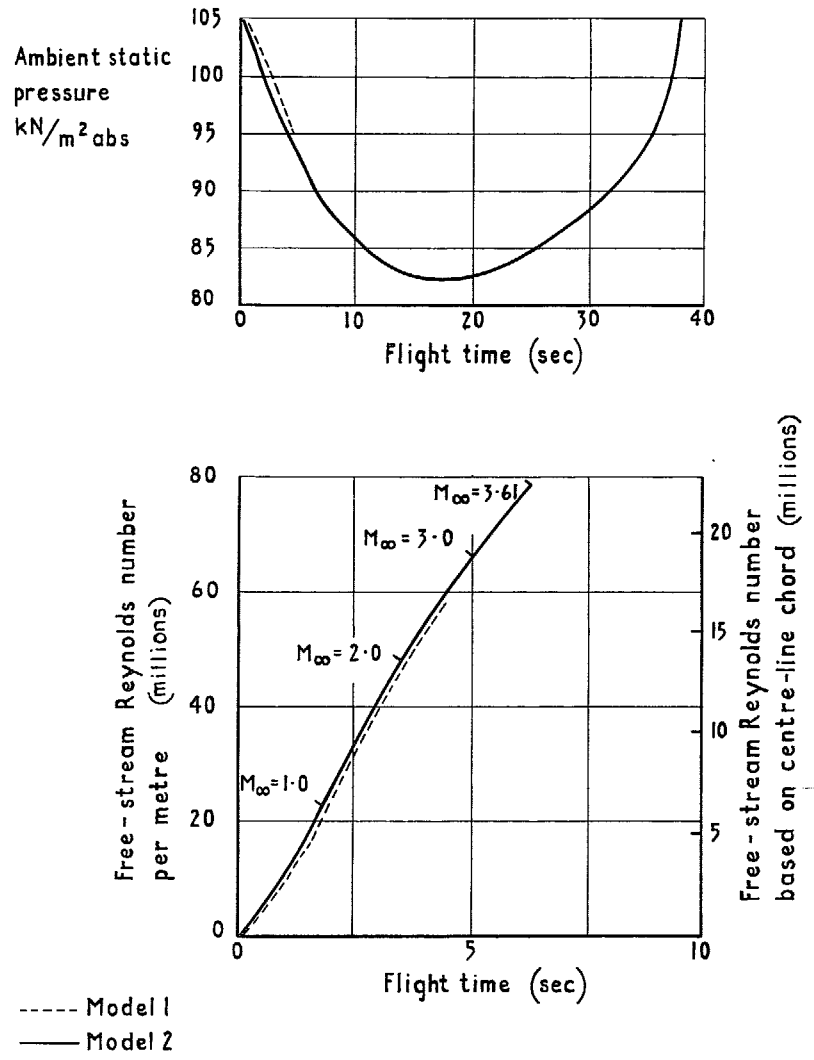

FIG 4 *contd.* Test conditions.

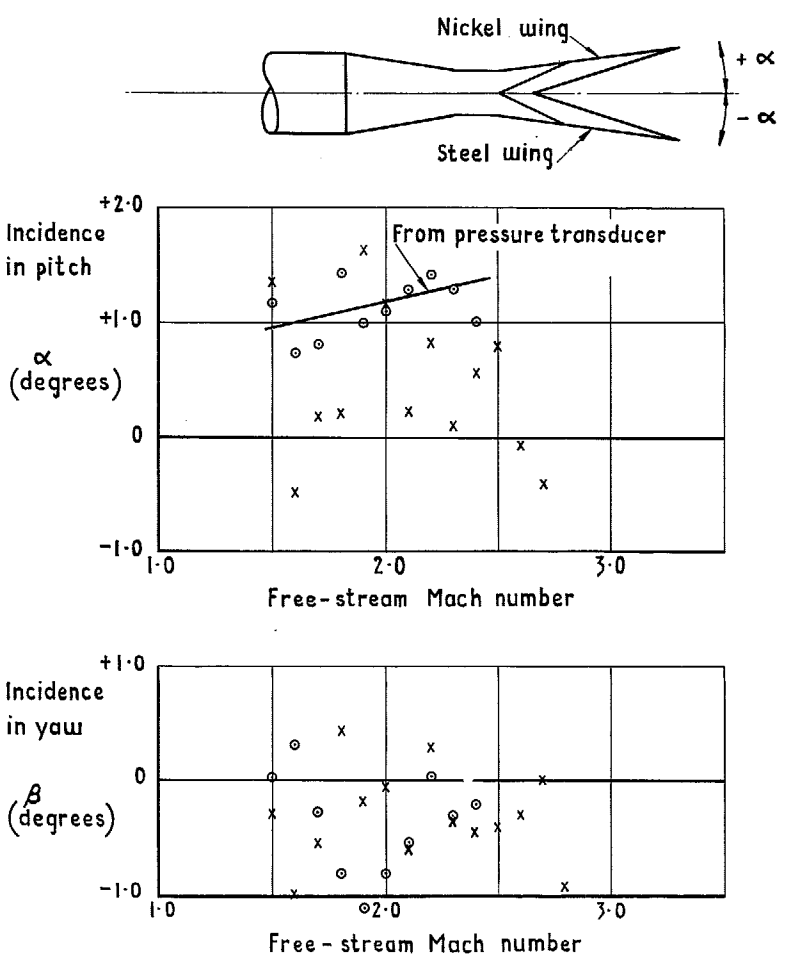

FIG. 5a. Inflight incidence in pitch and yaw—Model 1.

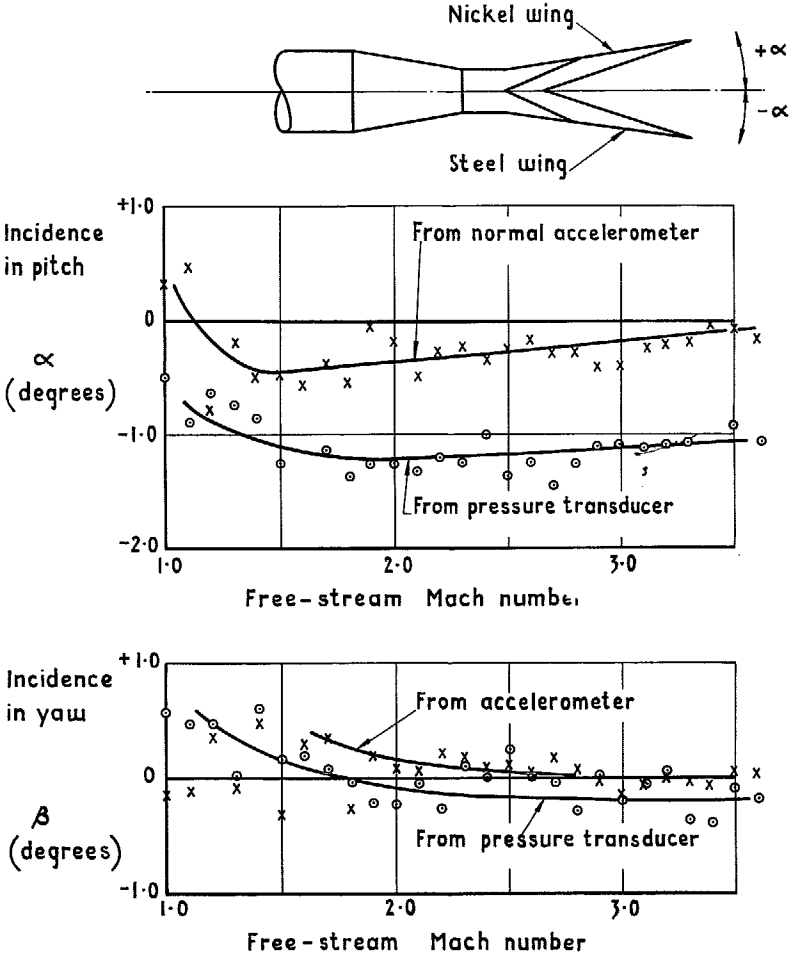

FIG. 5b. Inflight incidence in pitch and yaw—Model 2.

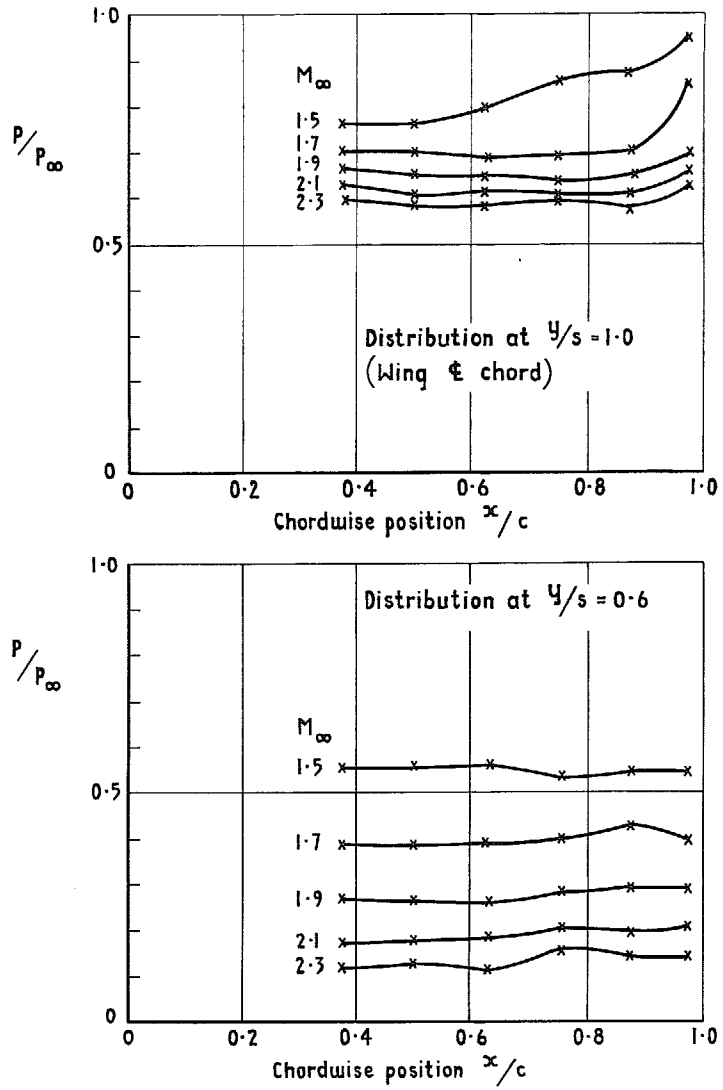

FIG. 6a. Chordwise variation of pressure at two spanwise stations—Model 1 (steel wing).

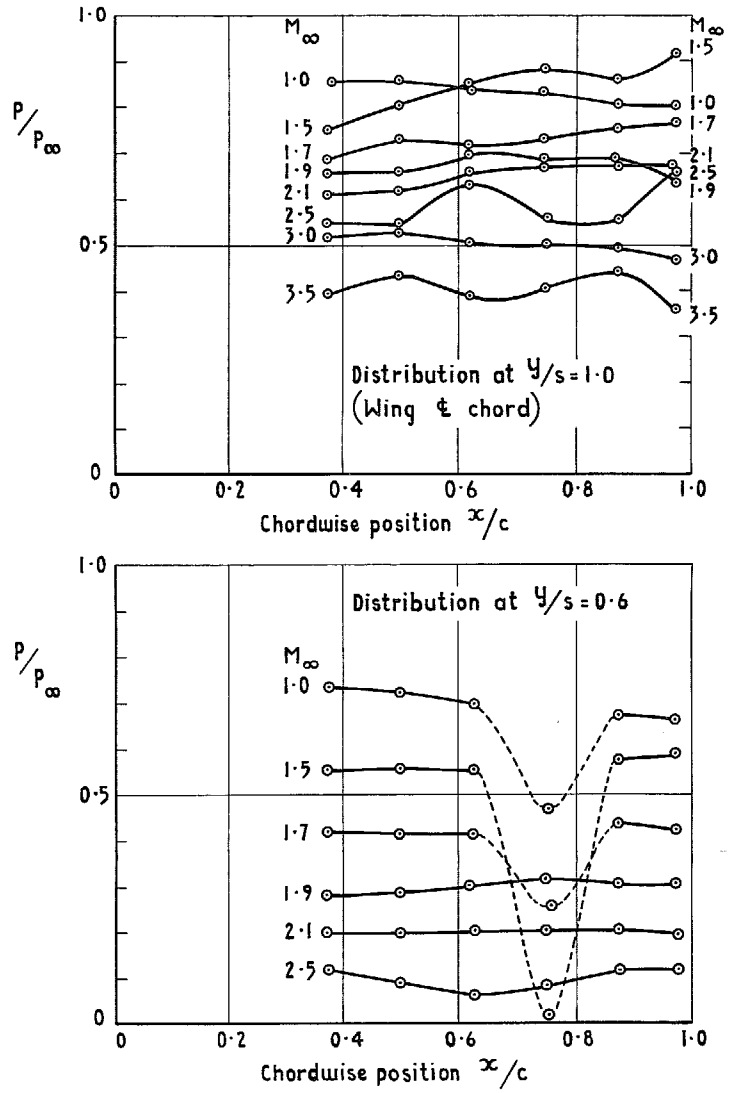

FIG. 6b. Chordwise variation of pressure at two spanwise stations—Model 2 (steel wing).

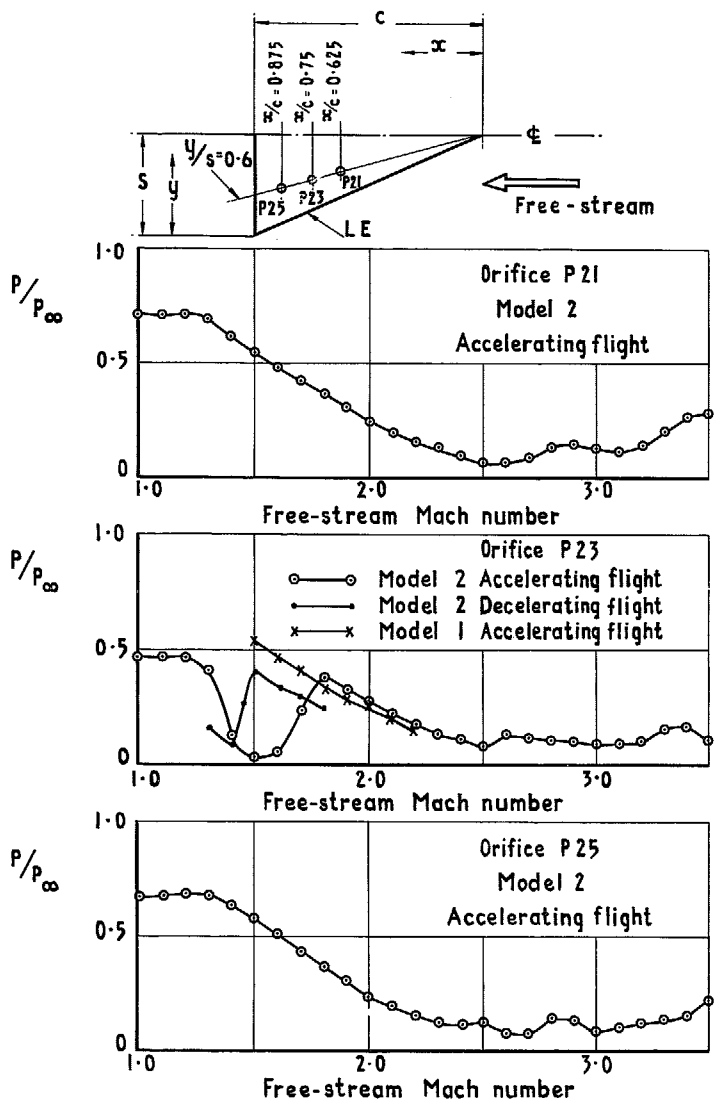

FIG. 7. Anomalous pressure at orifice *P*23 compared with adjacent stations (Model 2).

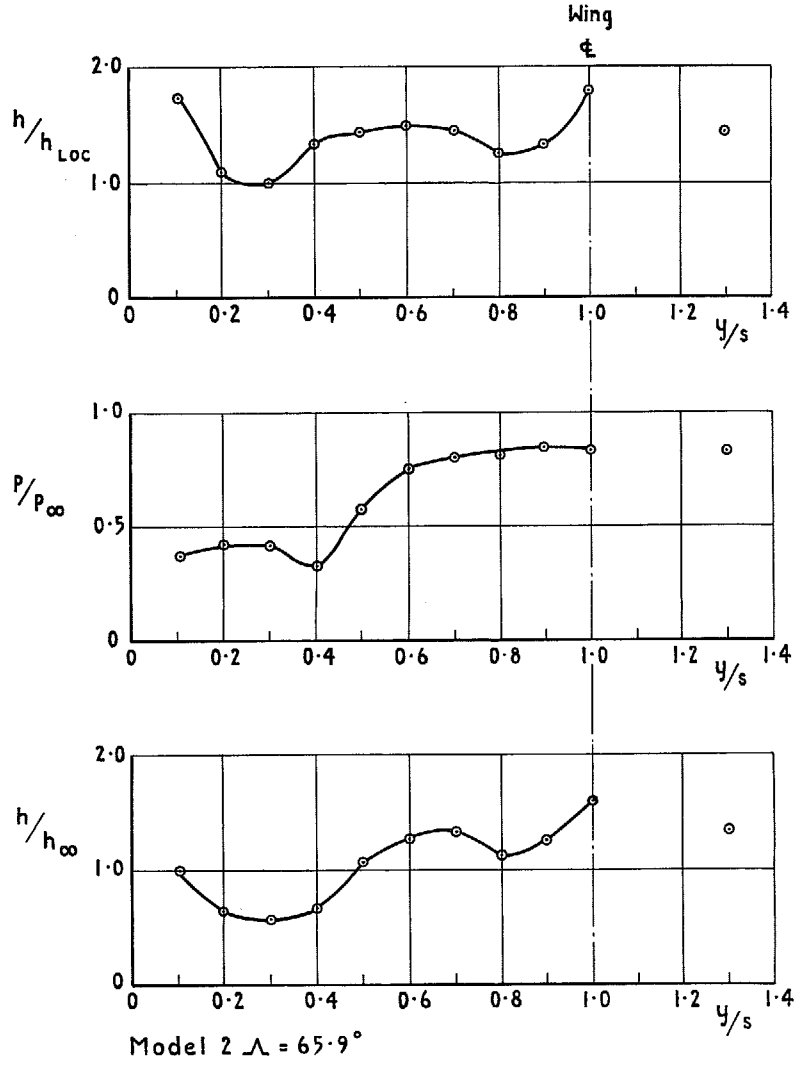

FIG. 8a. Spanwise distributions of heat transfer $\left(\frac{x}{c} = 0{\cdot}875\right)$ and pressure $\left(\frac{x}{c} = 0{\cdot}975\right)$ for nickel wing; $M_\infty = 1{\cdot}0$.

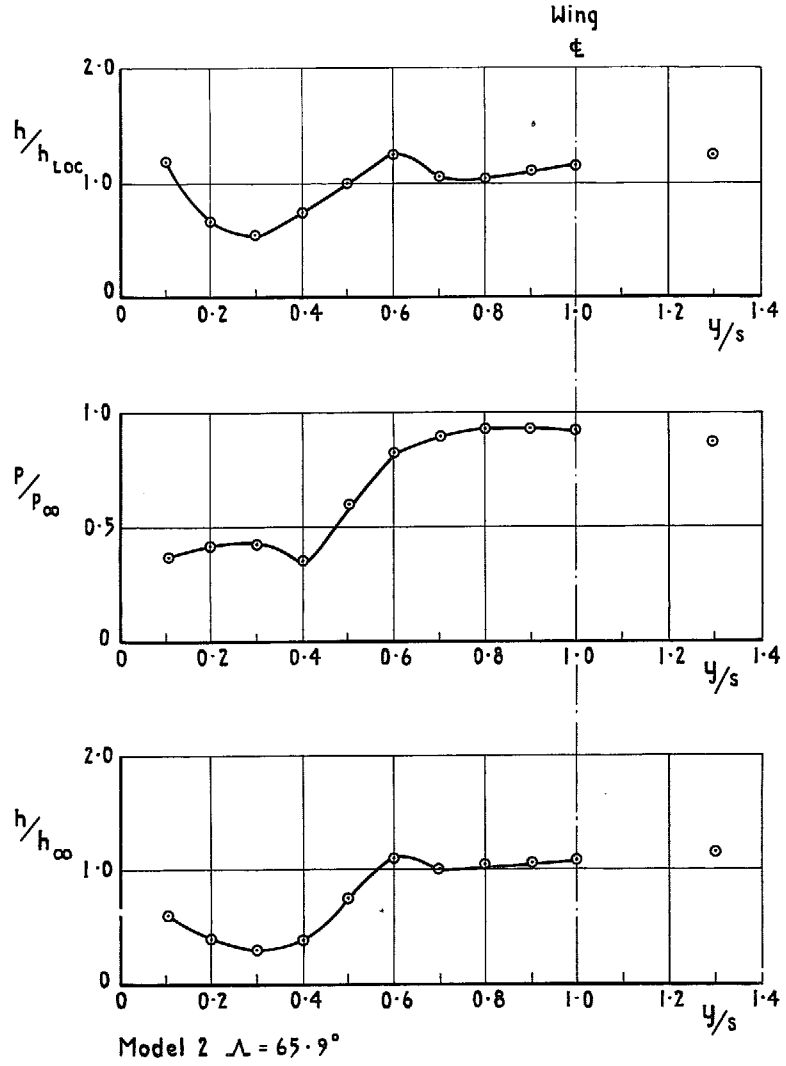

FIG. 8b. Spanwise distributions of heat transfer $\left(\frac{x}{c} = 0{\cdot}875\right)$ and pressure $\left(\frac{x}{c} = 0{\cdot}975\right)$ for nickel wing; $M_\infty = 1{\cdot}2$.

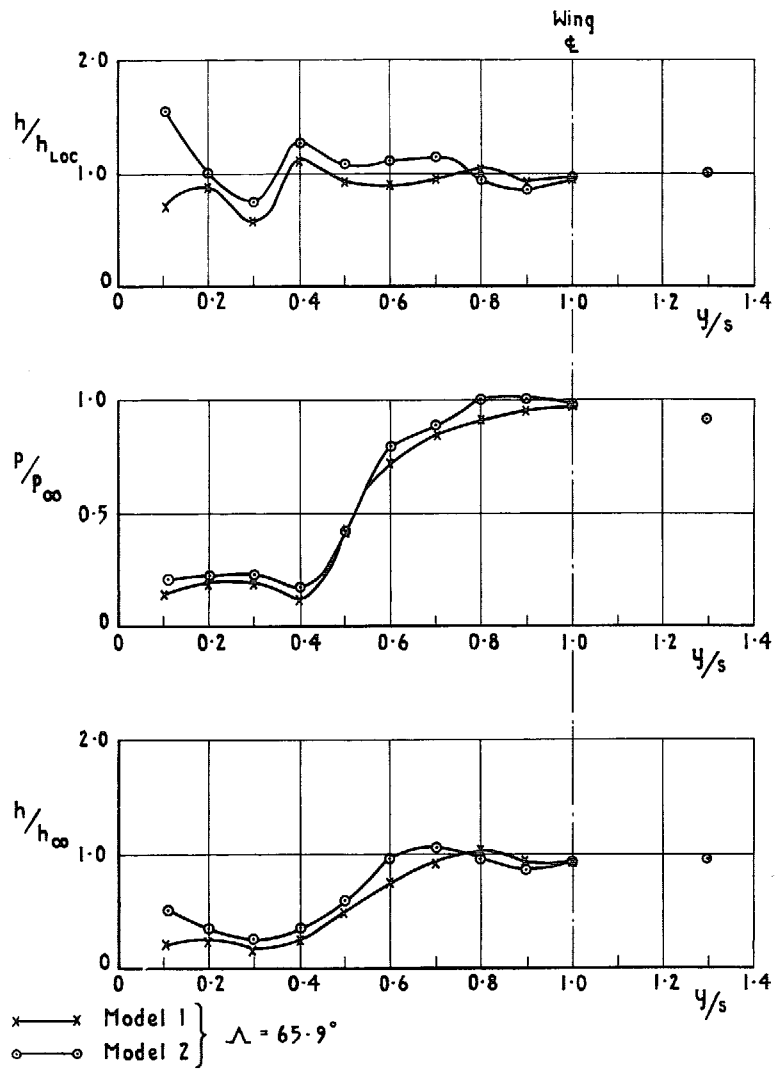

FIG. 8c. Spanwise distributions of heat transfer $\left(\frac{x}{c} = 0{\cdot}875\right)$ and pressure $\left(\frac{x}{c} = 0{\cdot}975\right)$ for nickel wing; $M_\infty = 1{\cdot}5$.

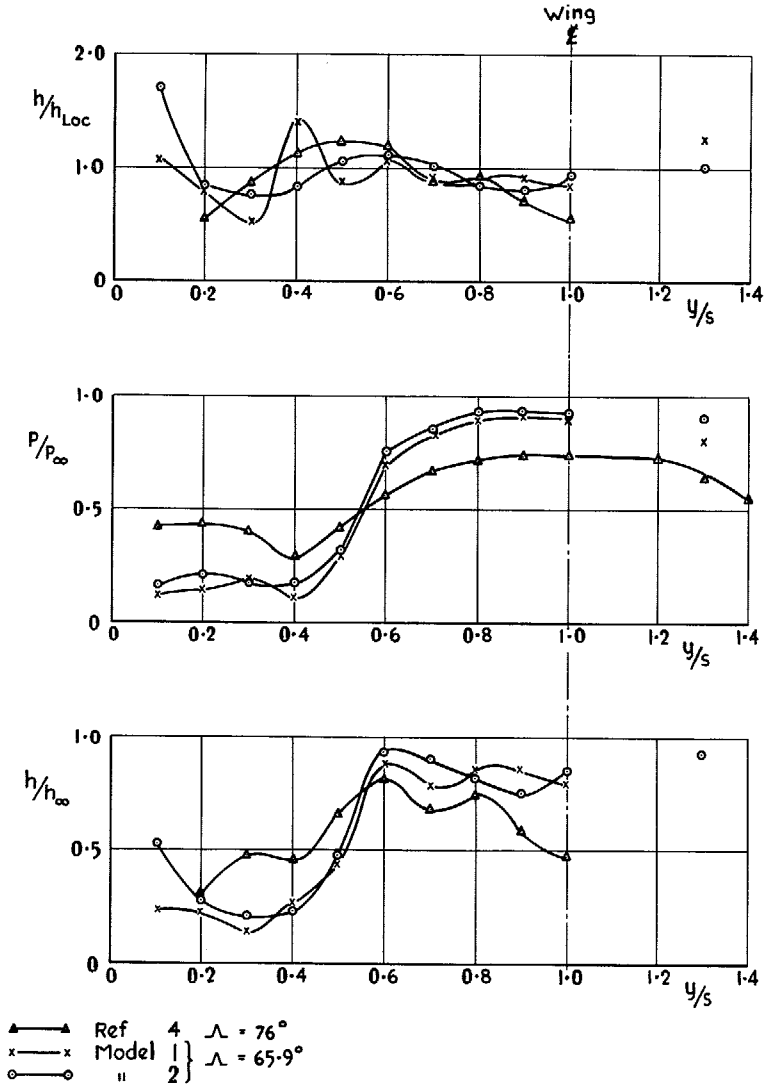

FIG. 8d. Spanwise distributions of heat transfer $\left(\frac{x}{c} = 0{\cdot}875\right)$ and pressure $\left(\frac{x}{c} = 0{\cdot}975\right)$ for nickel wing; $M_\infty = 1{\cdot}6$.

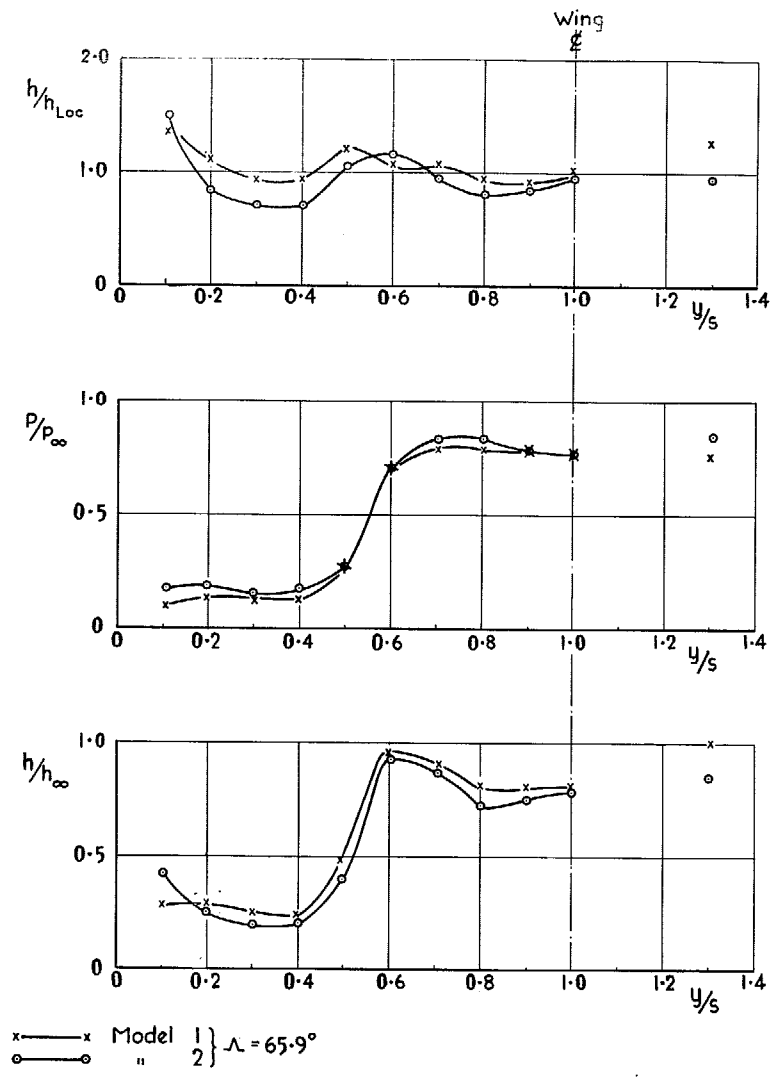

FIG. 8e. Spanwise distributions of heat transfer $\left(\frac{x}{c} = 0{\cdot}875\right)$ and pressure $\left(\frac{x}{c} = 0{\cdot}975\right)$ for nickel wing; $M_\infty = 1{\cdot}7$.

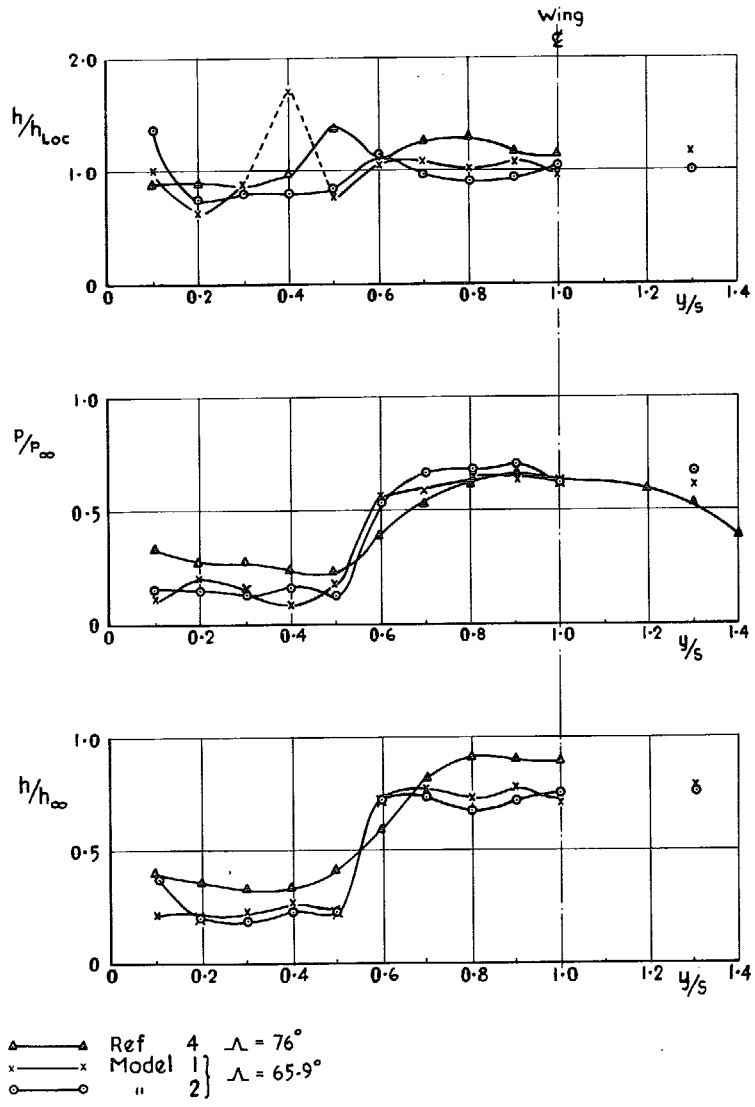

FIG. 8f. Spanwise distributions of heat transfer $\left(\frac{x}{c} = 0{\cdot}875\right)$ and pressure $\left(\frac{x}{c} = 0{\cdot}975\right)$ for nickel wing; $M_\infty = 2{\cdot}0$.

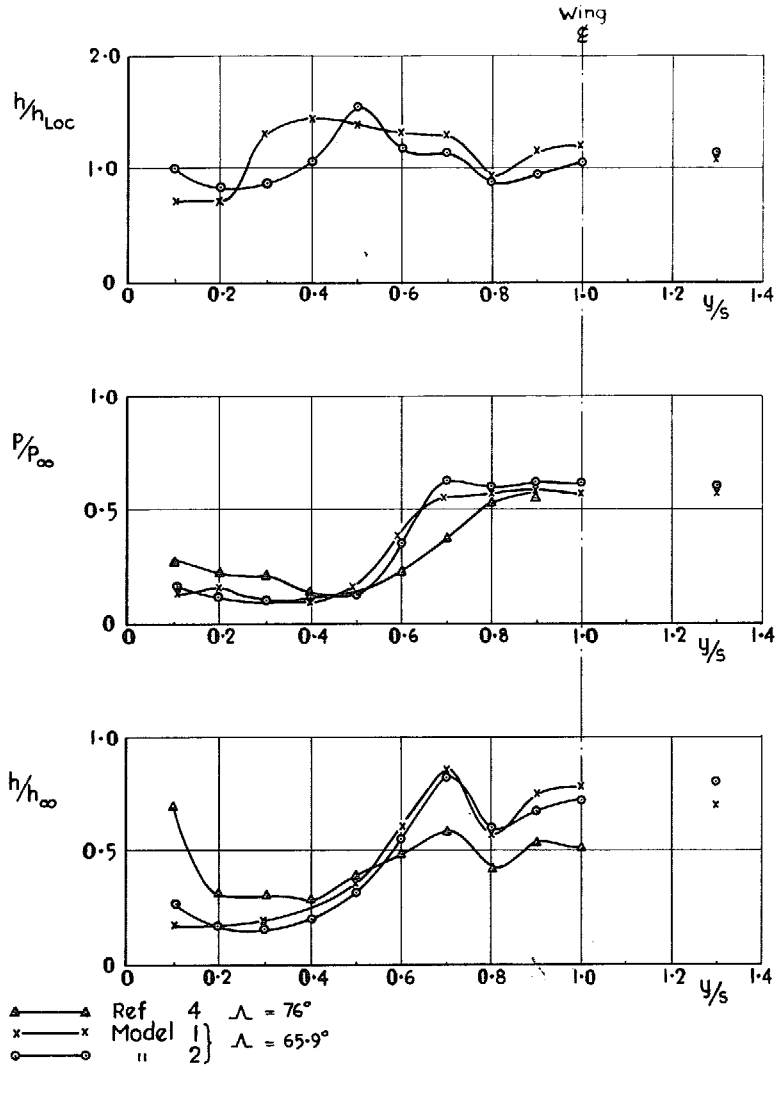

FIG. 8g. Spanwise distributions of heat transfer $\left(\frac{x}{c} = 0{\cdot}875\right)$ and pressure $\left(\frac{x}{c} = 0{\cdot}975\right)$ for nickel wing; $M_\infty = 2{\cdot}3$.

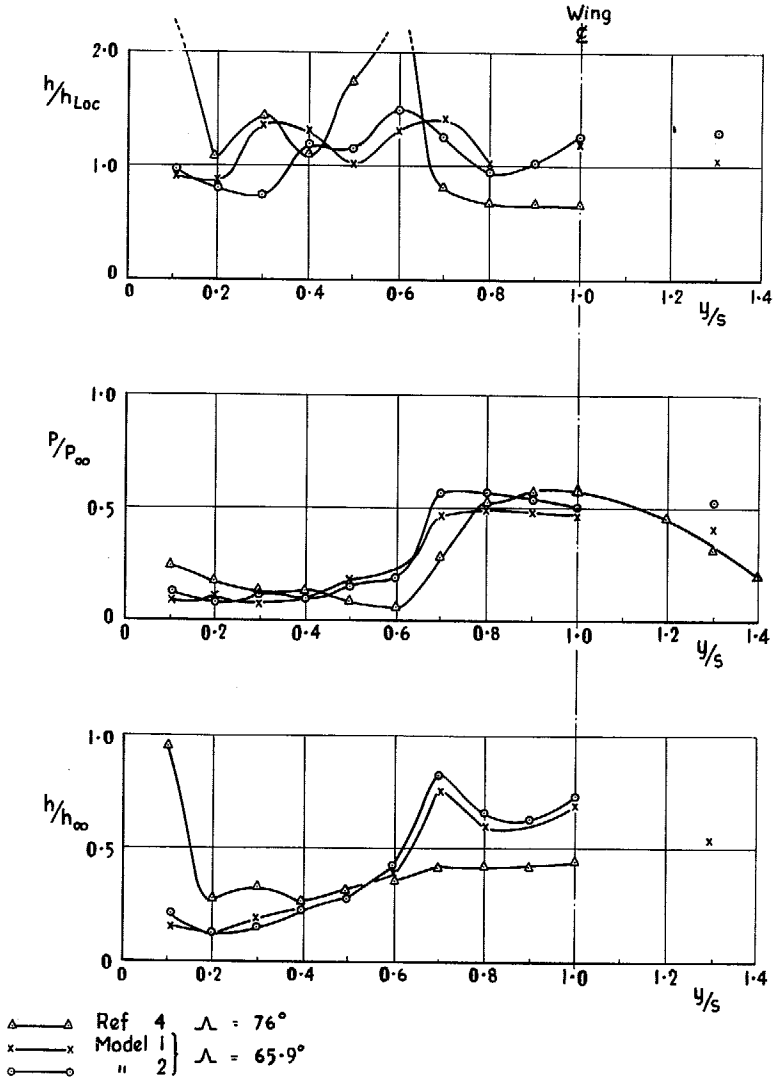

FIG. 8h. Spanwise distributions of heat transfer $\left(\frac{x}{c} = 0{\cdot}875\right)$ and pressure $\left(\frac{x}{c} = 0{\cdot}975\right)$ for nickel wing; $M_\infty = 2{\cdot}6$.

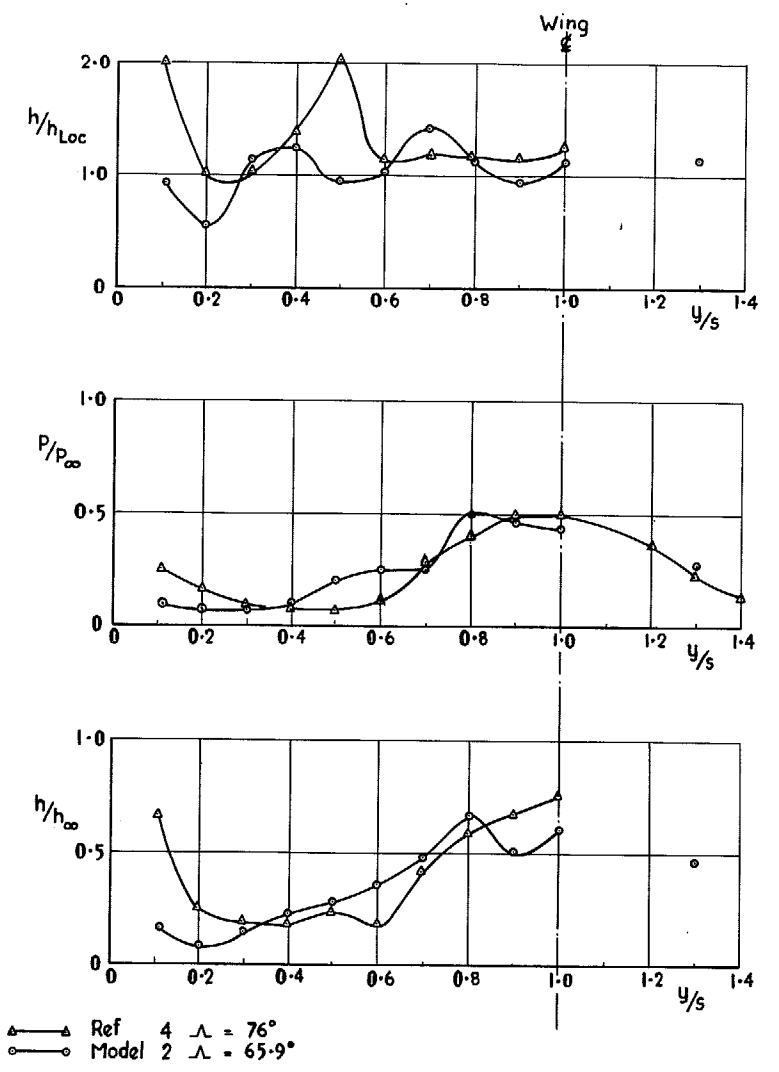

FIG. 8i. Spanwise distributions of heat transfer $\left(\frac{x}{c} = 0{\cdot}875\right)$ and pressure $\left(\frac{x}{c} = 0{\cdot}975\right)$ for nickel wing; $M_\infty = 3{\cdot}0$.

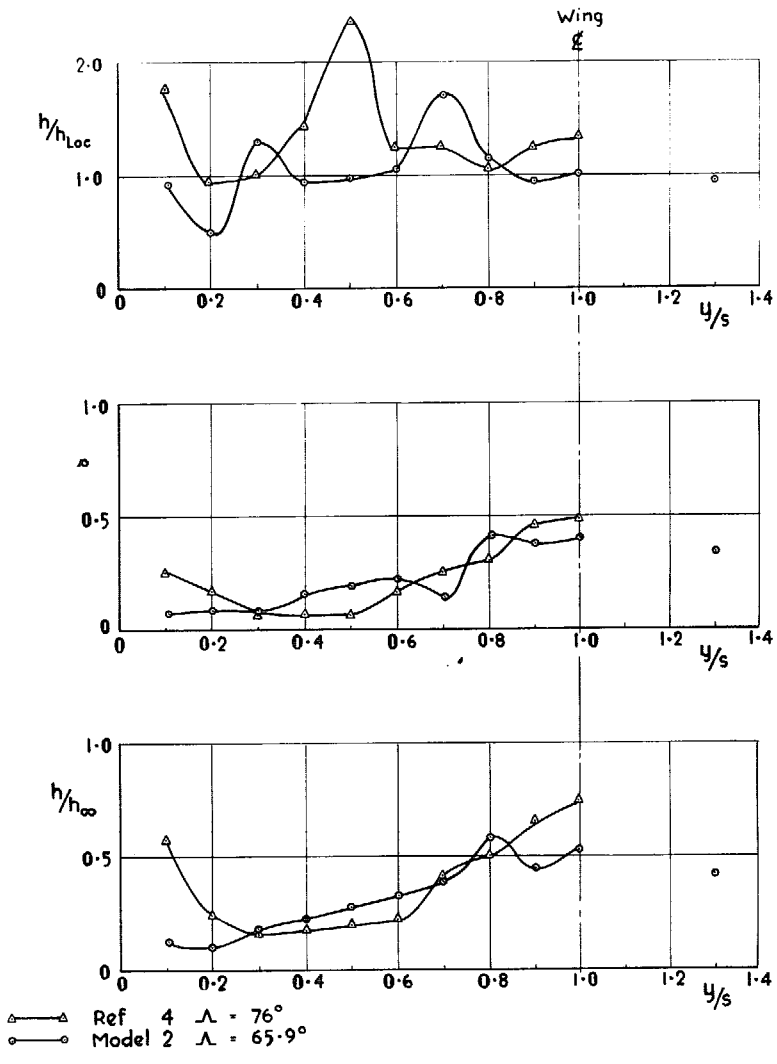

FIG. 8j. Spanwise distributions of heat transfer $\left(\frac{x}{c} = 0{\cdot}875\right)$ and pressure $\left(\frac{x}{c} = 0{\cdot}975\right)$ for nickel wing; $M_\infty = 3{\cdot}2$.

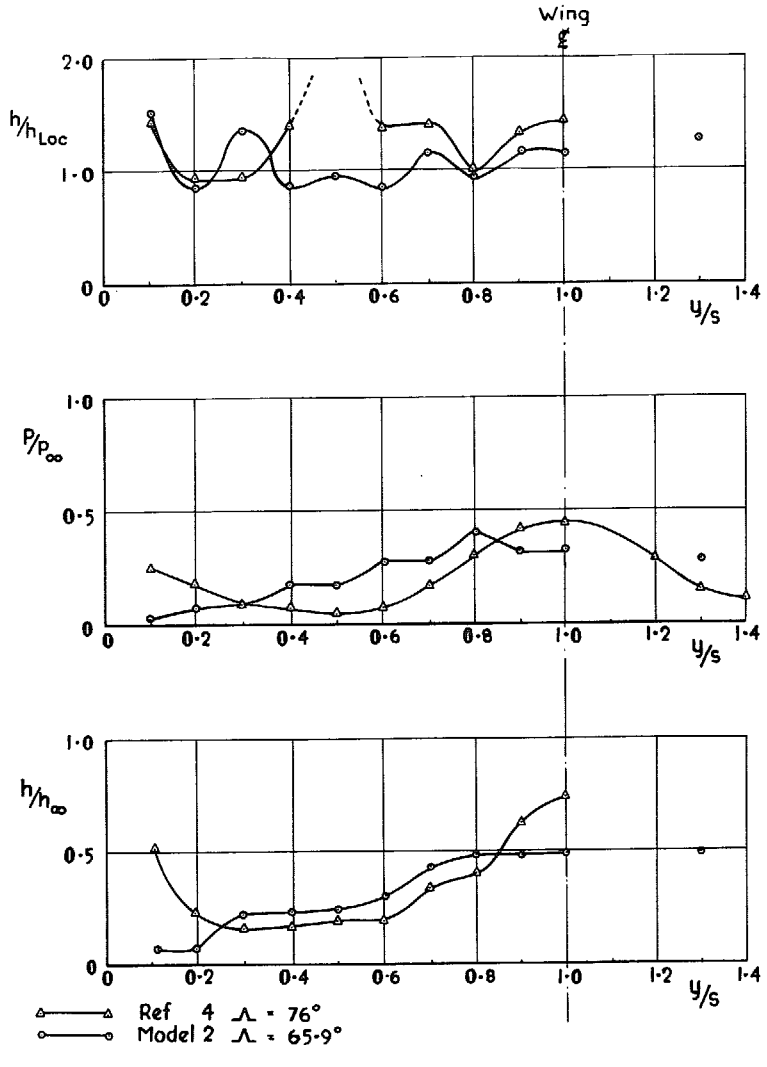

FIG. 8k. Spanwise distributions of heat transfer $\left(\frac{x}{c} = 0{\cdot}875\right)$ and pressure $\left(\frac{x}{c} = 0{\cdot}975\right)$ for nickel wing; $M_\infty = 3{\cdot}4$.

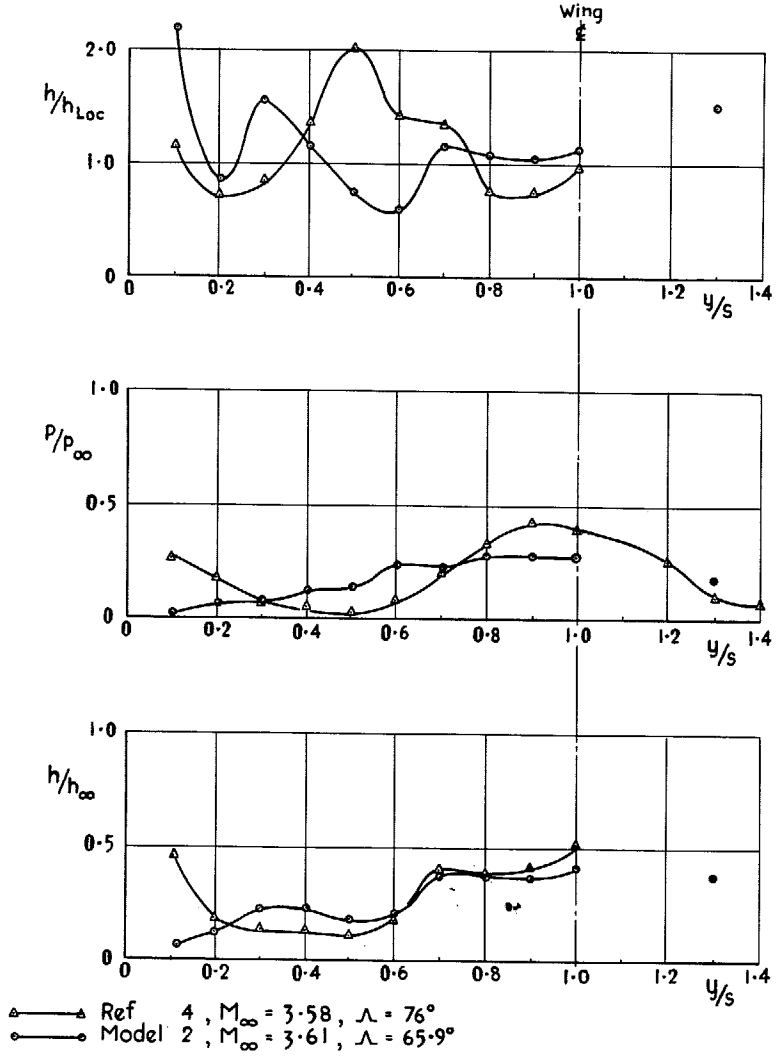

FIG. 8l. Spanwise distributions of heat transfer $\left(\frac{x}{c} = 0{\cdot}875\right)$ and pressure $\left(\frac{x}{c} = 0{\cdot}975\right)$ for nickel wing; $M_\infty = 3{\cdot}58/3{\cdot}61$.

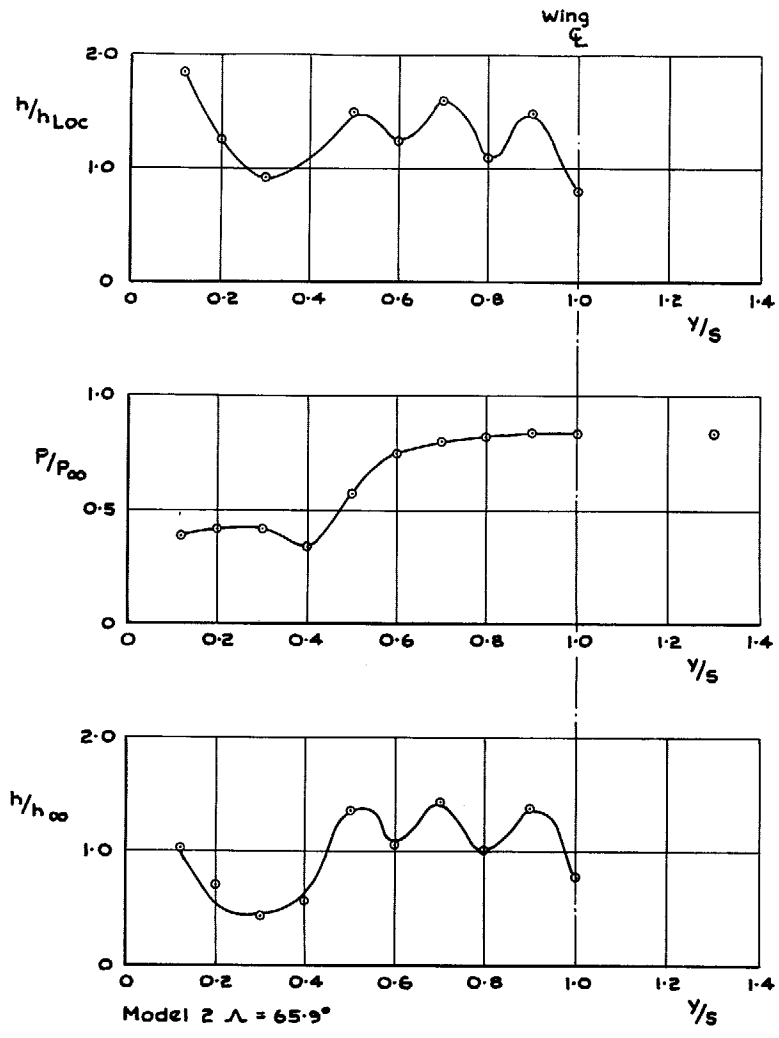

FIG. 9a. Spanwise distributions of heat transfer $\left(\frac{x}{c} = 0{\cdot}75\right)$ and pressure $\left(\frac{x}{c} = 0{\cdot}975\right)$ for nickel wing; $M_\infty = 1{\cdot}0$.

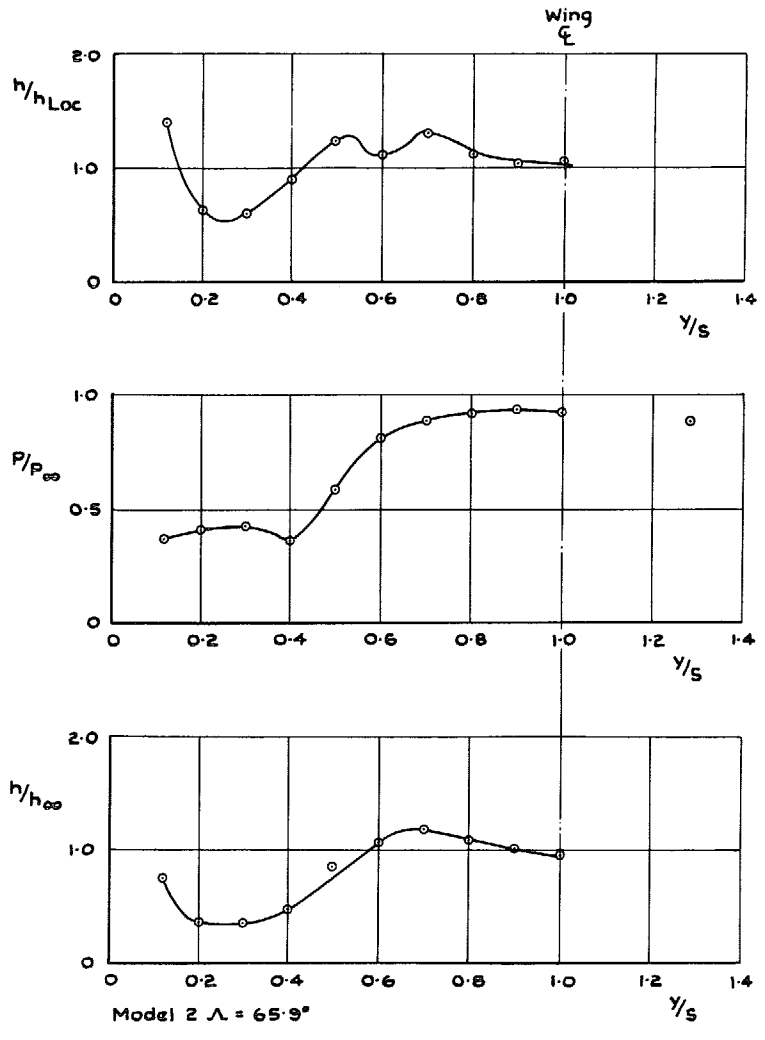

Fig. 9b. Spanwise distributions of heat transfer $\left(\frac{x}{c} = 0{\cdot}75\right)$ and pressure $\left(\frac{x}{c} = 0{\cdot}975\right)$ for nickel wing; $M_\infty = 1{\cdot}2$.

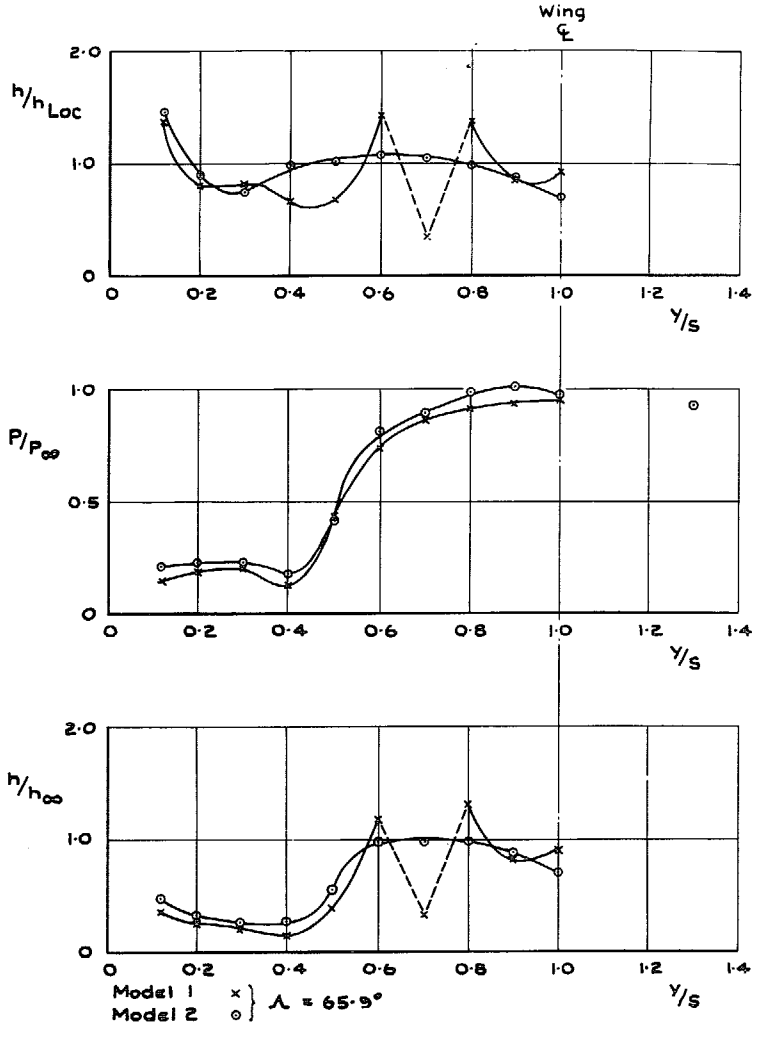

FIG. 9c. Spanwise distributions of heat transfer $\left(\frac{x}{c} = 0{\cdot}75\right)$ and pressure $\left(\frac{x}{c} = 0{\cdot}975\right)$ for nickel wing; $M_\infty = 1{\cdot}5$.

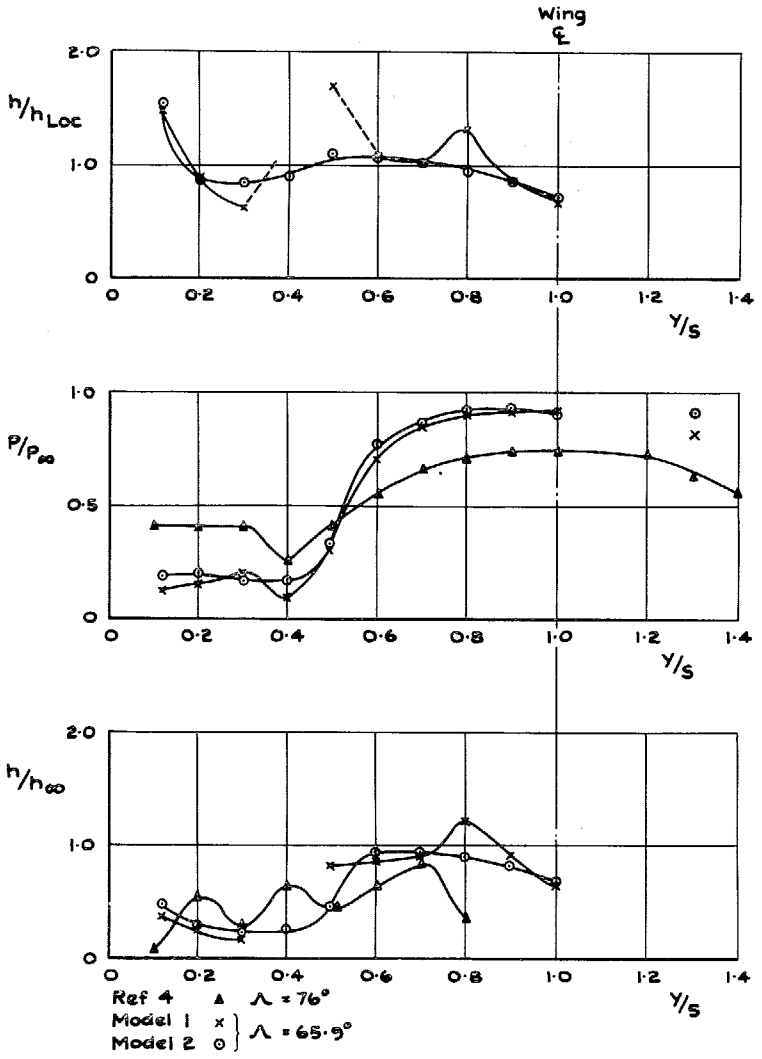

FIG. 9d. Spanwise distributions of heat transfer $\left(\frac{x}{c} = 0{\cdot}75\right)$ and pressure $\left(\frac{x}{c} = 0{\cdot}975\right)$ for nickel wing; $M_\infty = 1{\cdot}6$.

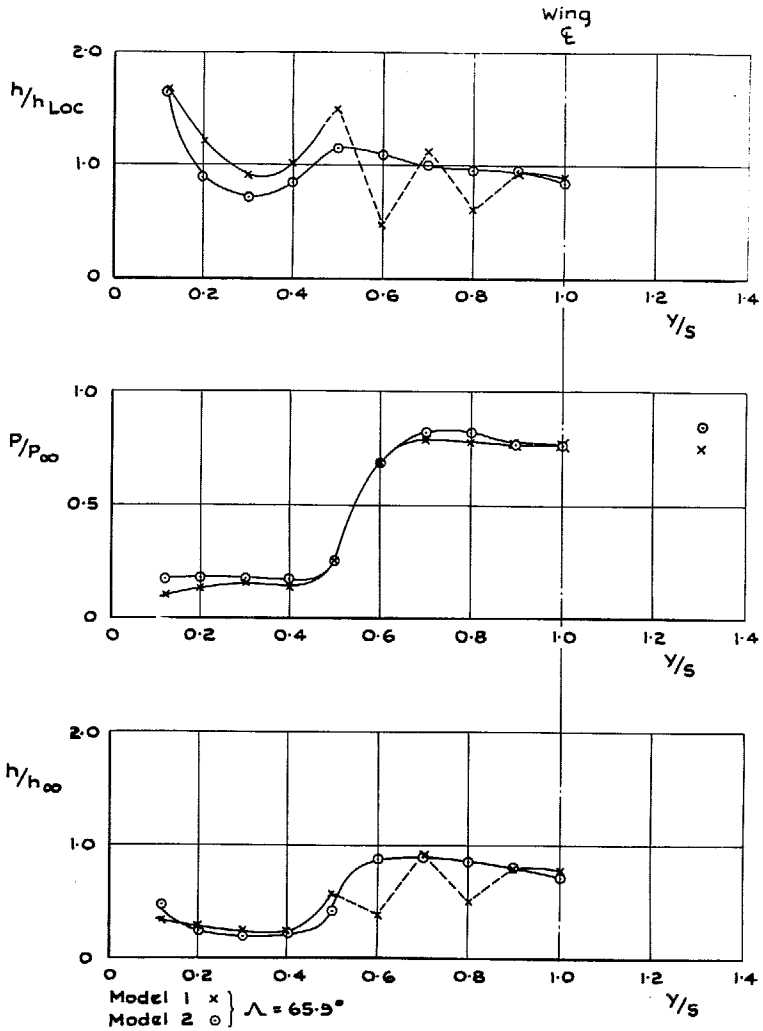

FIG. 9e. Spanwise distributions of heat transfer $\left(\frac{x}{c} = 0{\cdot}75\right)$ and pressure $\left(\frac{x}{c} = 0{\cdot}975\right)$ for nickel wing; $M_\infty = 1{\cdot}7$.

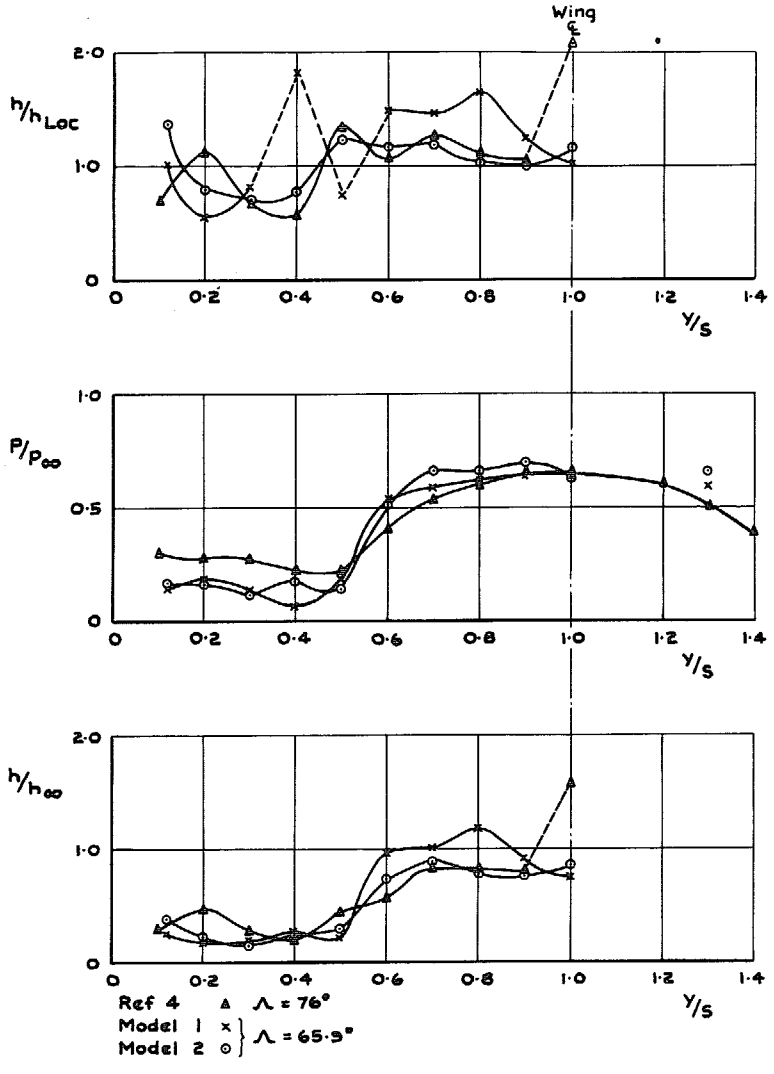

FIG. 9f. Spanwise distributions of heat transfer $\left(\frac{x}{c} = 0{\cdot}75\right)$ and pressure $\left(\frac{x}{c} = 0{\cdot}975\right)$ for nickel wing; $M_{\infty} = 2{\cdot}0$.

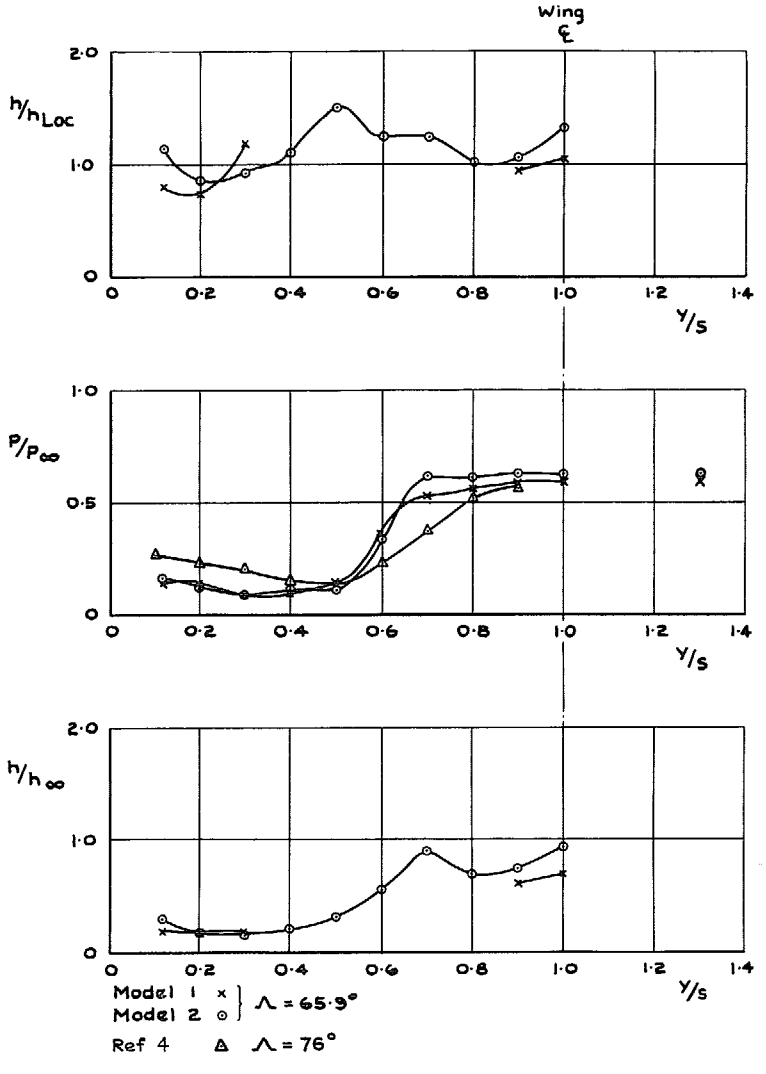

FIG. 9g. Spanwise distributions of heat transfer $\left(\frac{x}{c} = 0{\cdot}75\right)$ and pressure $\left(\frac{x}{c} = 0{\cdot}975\right)$ for nickel wing; $M_{\infty} = 2{\cdot}3$.

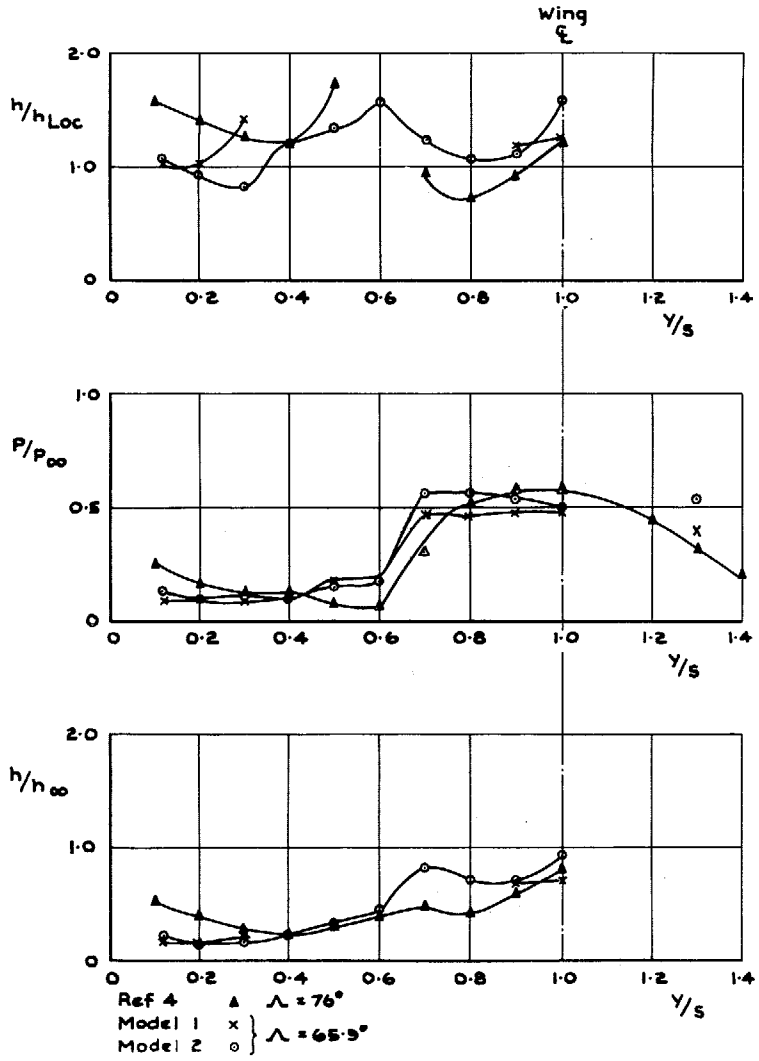

FIG. 9h. Spanwise distributions of heat transfer $\left(\frac{x}{c} = 0{\cdot}75\right)$ and pressure $\left(\frac{x}{c} = 0{\cdot}975\right)$ for nickel wing; $M_\infty = 2{\cdot}6$.

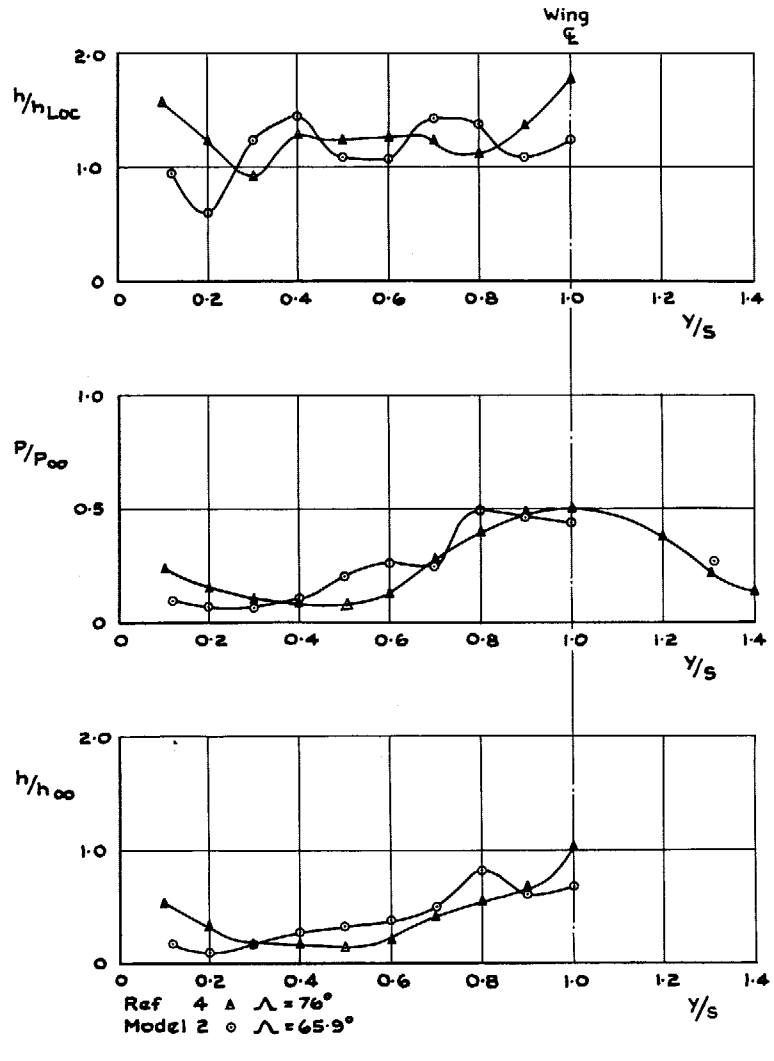

FIG. 9i. Spanwise distributions of heat transfer $\left(\frac{x}{c} = 0{\cdot}75\right)$ and pressure $\left(\frac{x}{c} = 0{\cdot}975\right)$ for nickel wing; $M_\infty = 3{\cdot}0$.

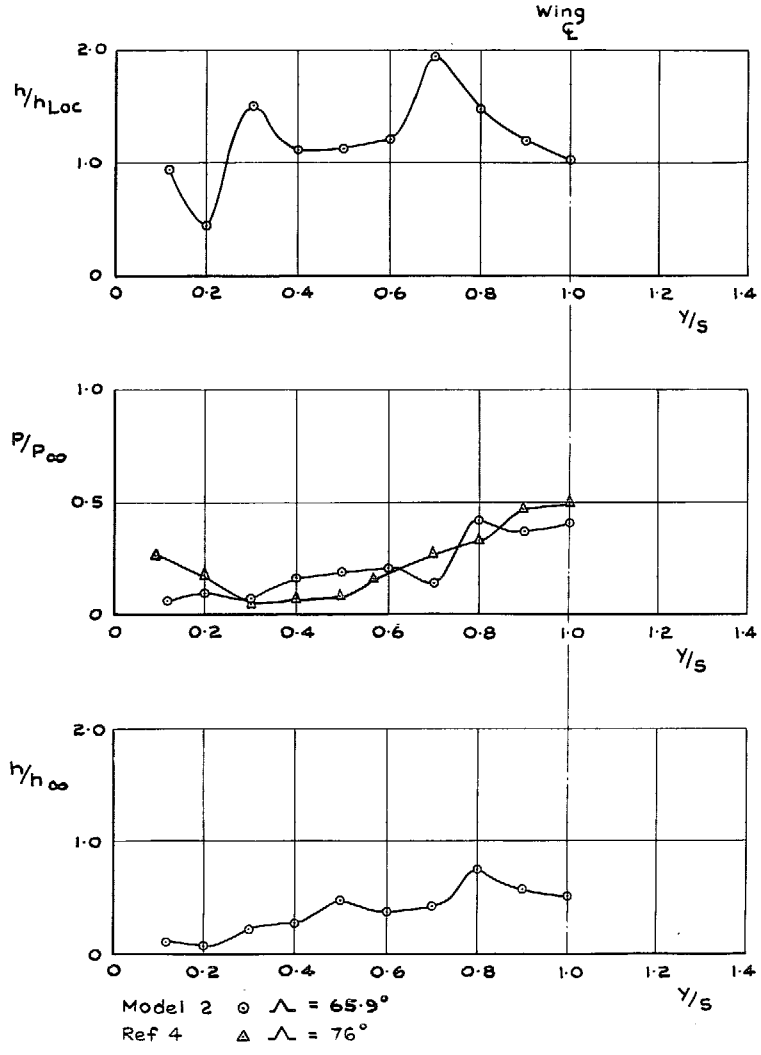

FIG. 9j. Spanwise distributions of heat transfer $\left(\frac{x}{c} = 0{\cdot}75\right)$ and pressure $\left(\frac{x}{c} = 0{\cdot}975\right)$ for nickel wing; $M_\infty = 3{\cdot}2$.

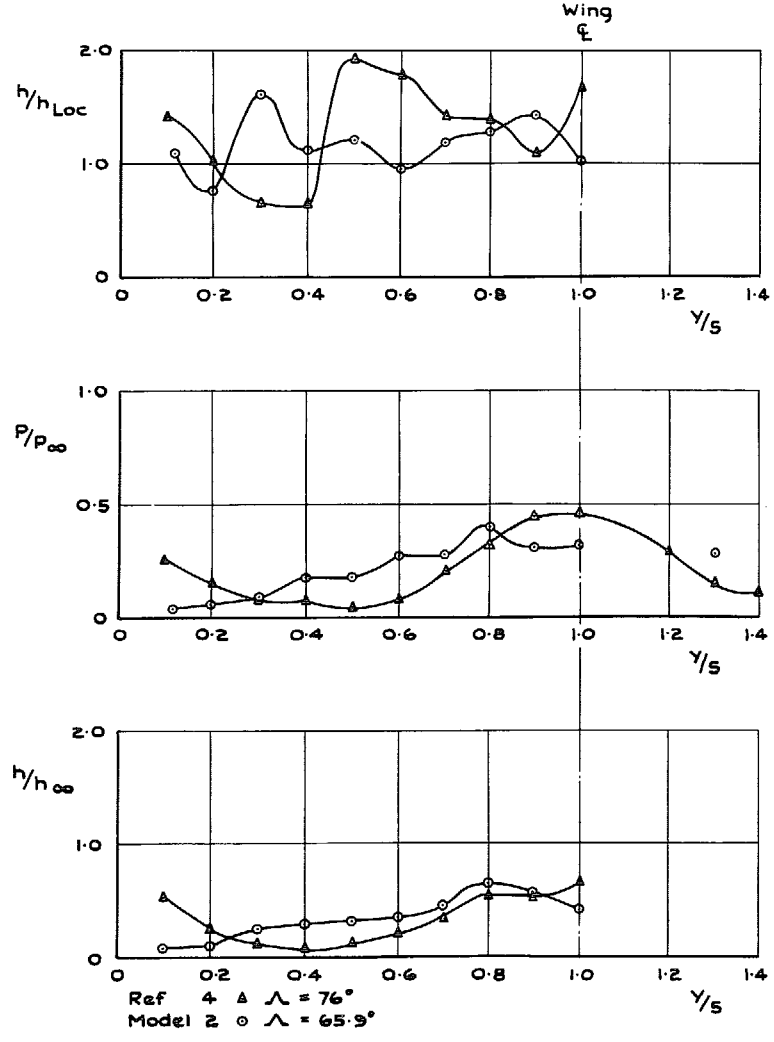

FIG. 9k. Spanwise distributions of heat transfer $\left(\frac{x}{c} = 0{\cdot}75\right)$ and pressure $\left(\frac{x}{c} = 0{\cdot}975\right)$ for nickel wing; $M_\infty = 3{\cdot}4$.

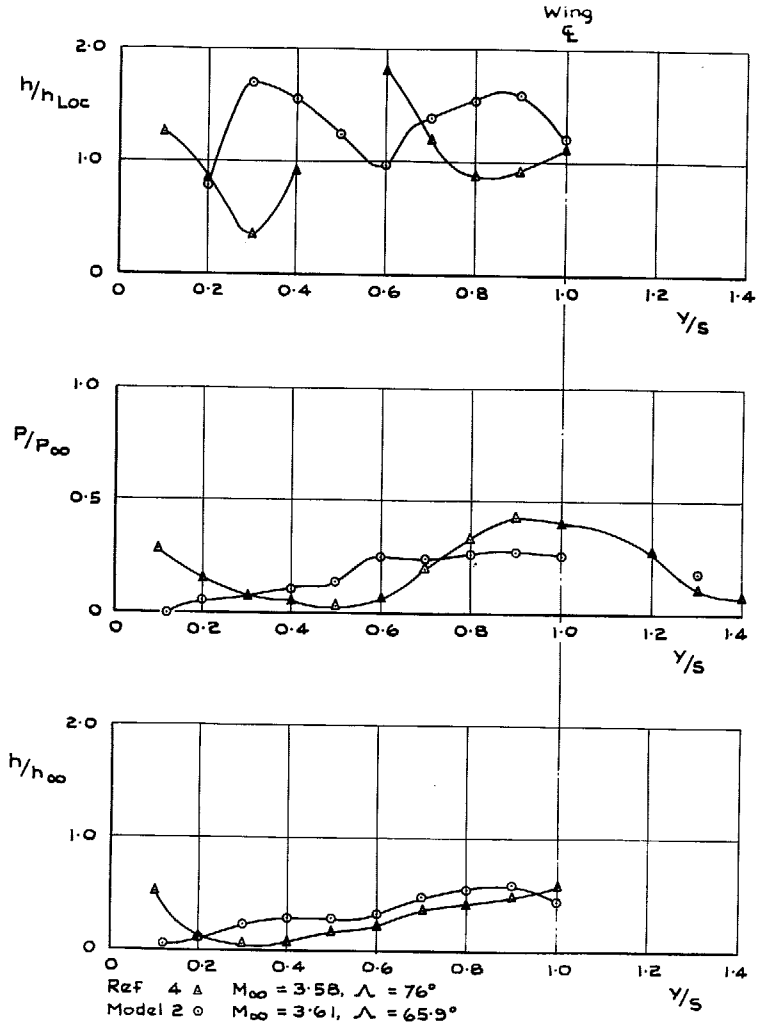

FIG. 9. Spanwise distributions of heat transfer $\left(\frac{x}{c} = 0{\cdot}75\right)$ and pressure $\left(\frac{x}{c} = 0{\cdot}975\right)$ for nickel wing: $M_\infty = 3{\cdot}58/3{\cdot}61$.

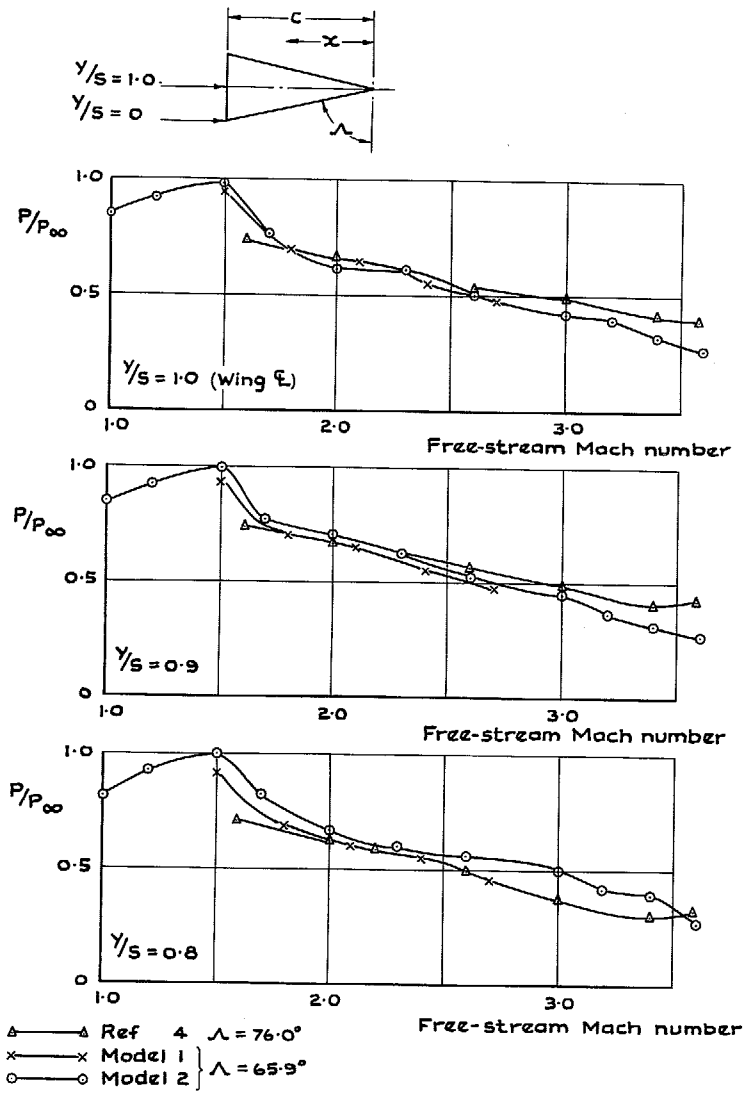

FIG. 10. Variation of pressure at spanwise stations with Mach number ($x/c = 0{\cdot}975$).

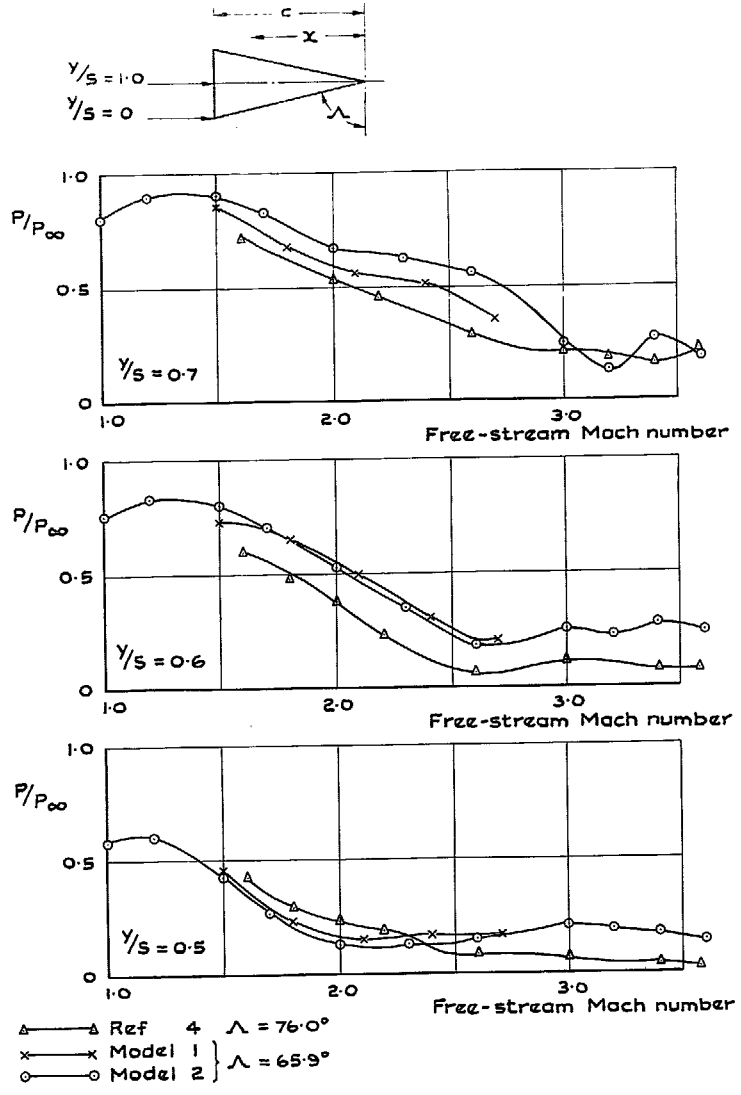

FIG. 10 *contd.* Variation of pressure at spanwise stations with Mach number ($x/c = 0{\cdot}975$).

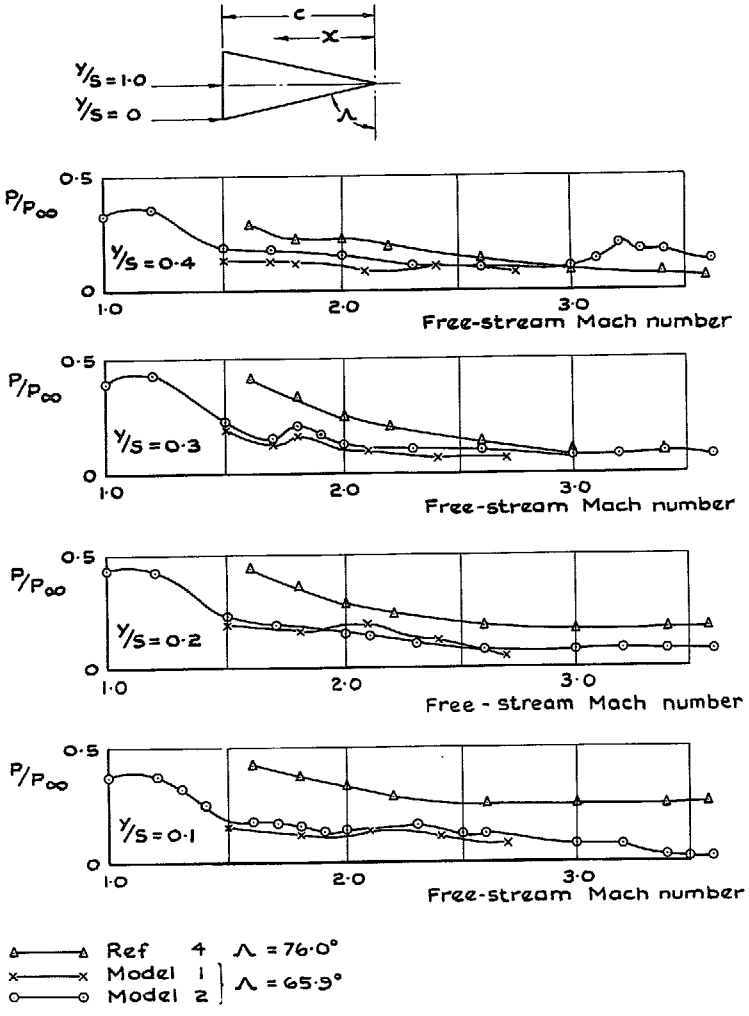

FIG. 10 *concld.* Variation of pressure at spanwise stations with Mach number ($x/c = 0{\cdot}975$).

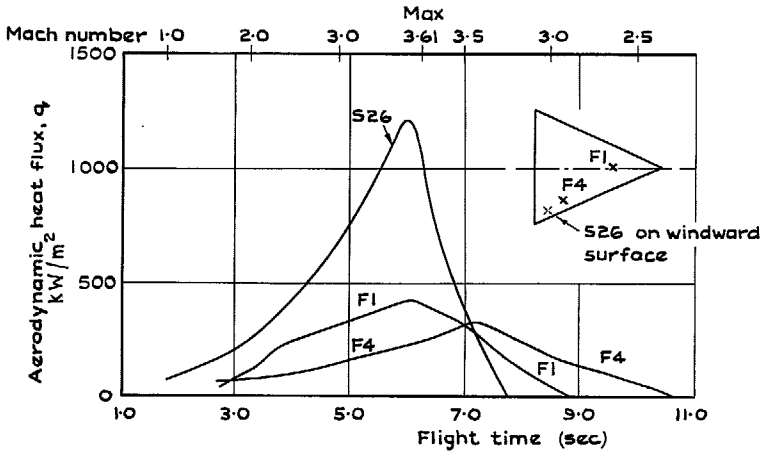

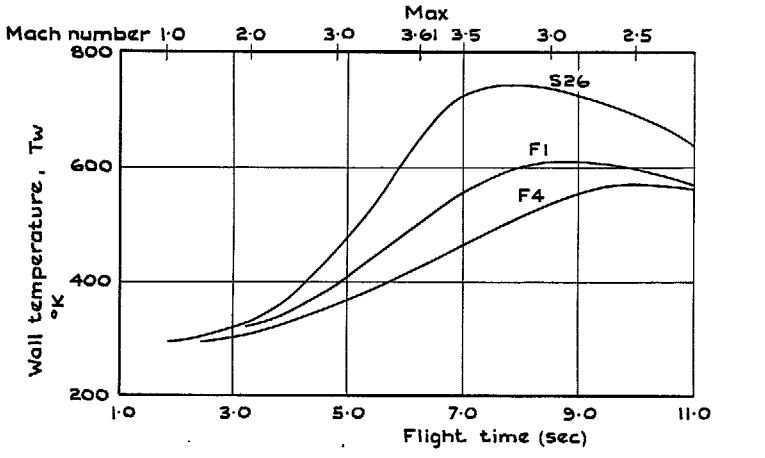

Note: Initial letter F = fast sampling (80 Hz) thermocouple
Initial letter S = slow sampling ($6\frac{2}{3}$ Hz) thermocouple

FIG. 11. Variations of heat flux and wall temperature with flight time at three stations on Model 2.

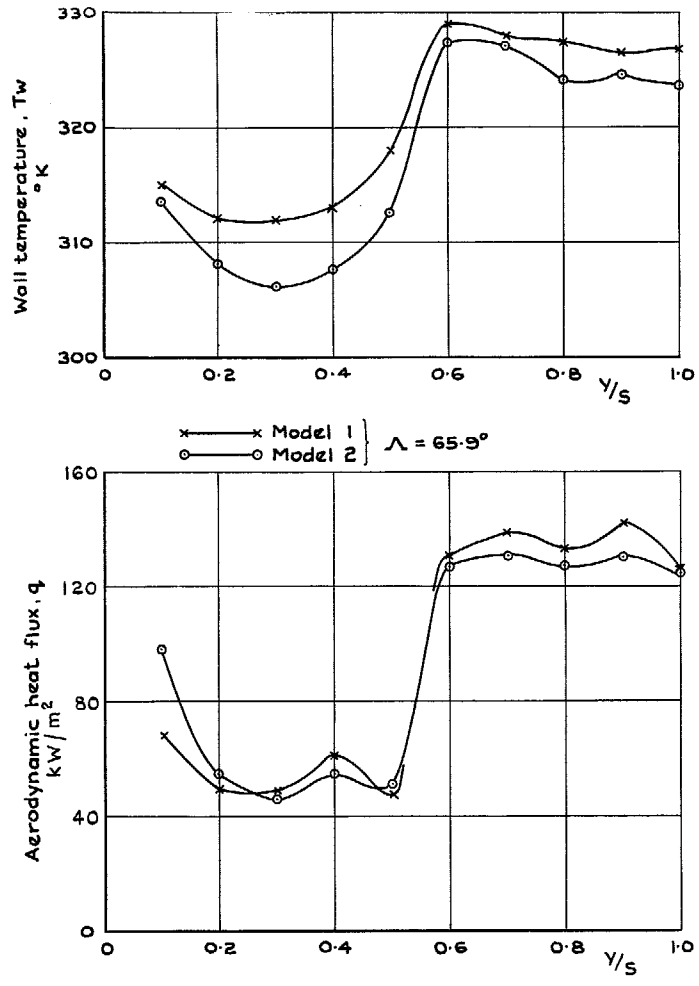

FIG. 12a. Spanwise wall temperature and heat flux distributions; $x/c = 0{\cdot}875$; $M_\infty = 2{\cdot}0$.

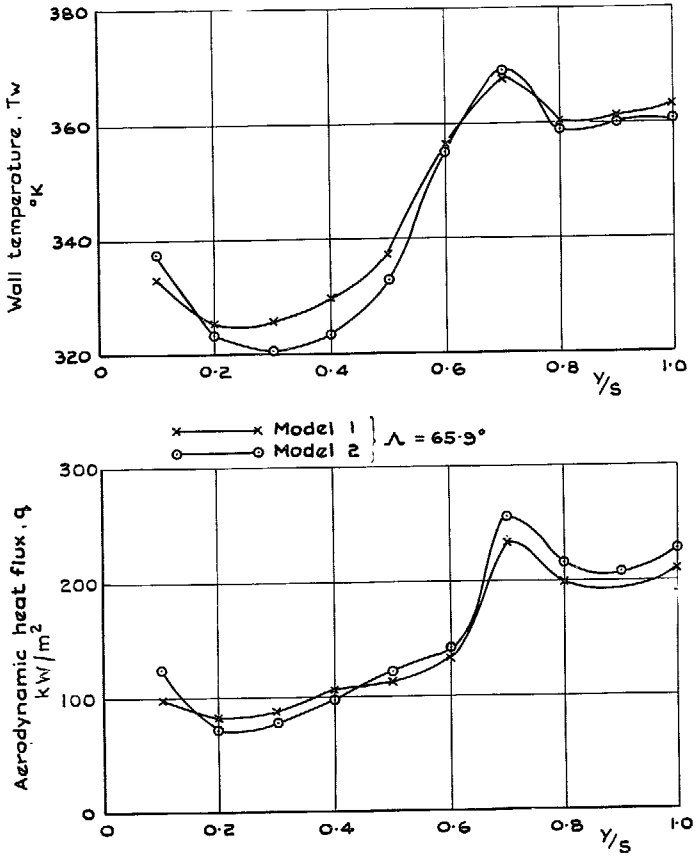

FIG. 12b. Spanwise wall temperature and heat flux distributions; $x/c = 0{\cdot}875$; $M_\infty = 2{\cdot}6$.

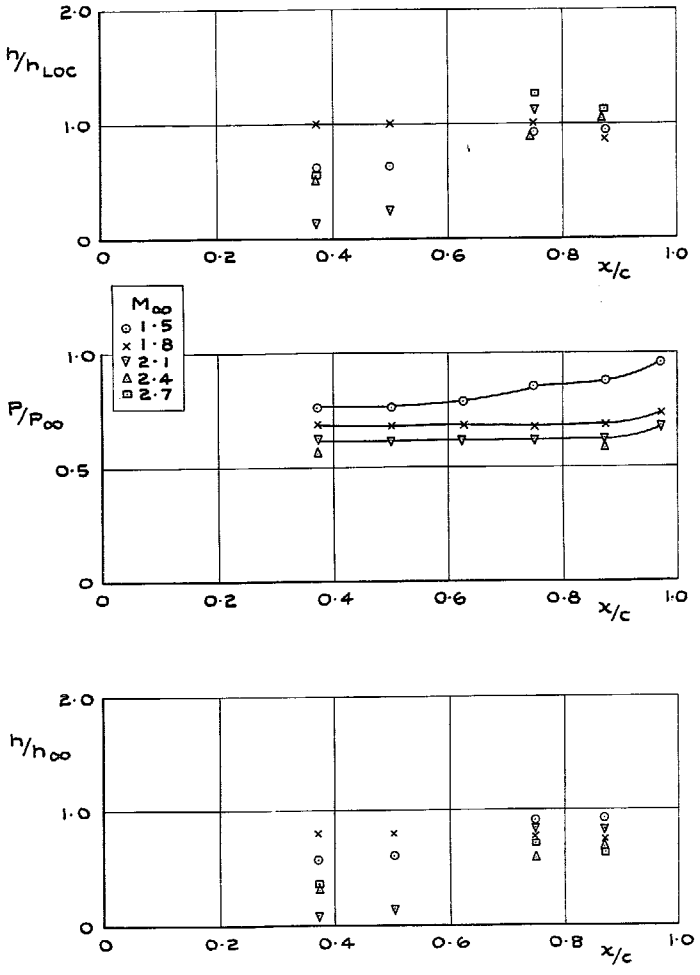

FIG. 13a. Variation of heat transfer and pressure along centreline of wing—Model 1.

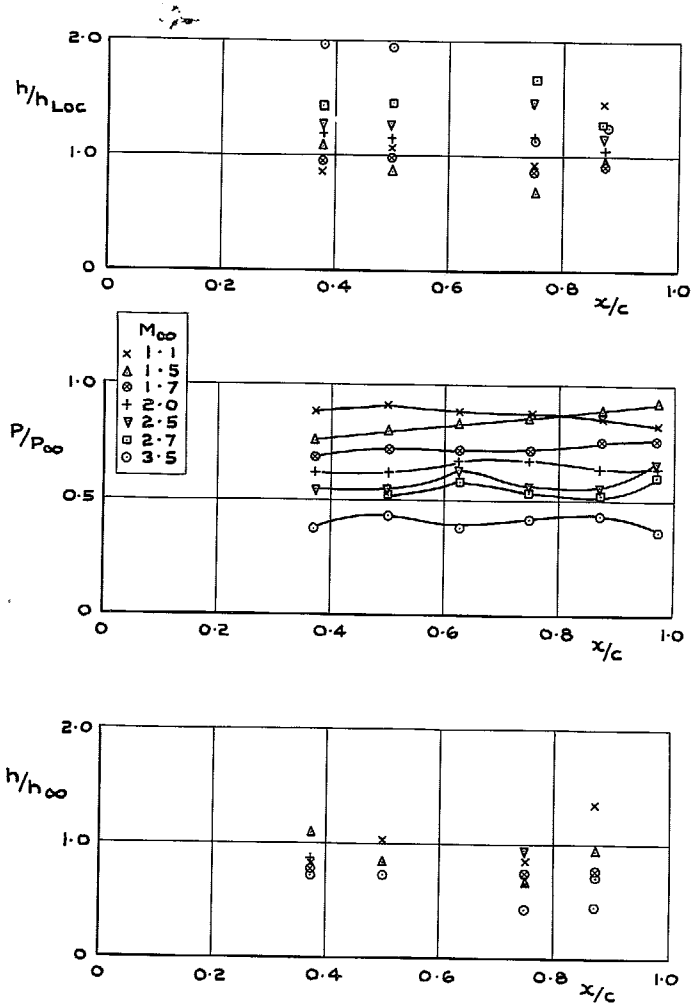

FIG. 13b. Variation of heat transfer and pressure along centreline of wing—Model 2.

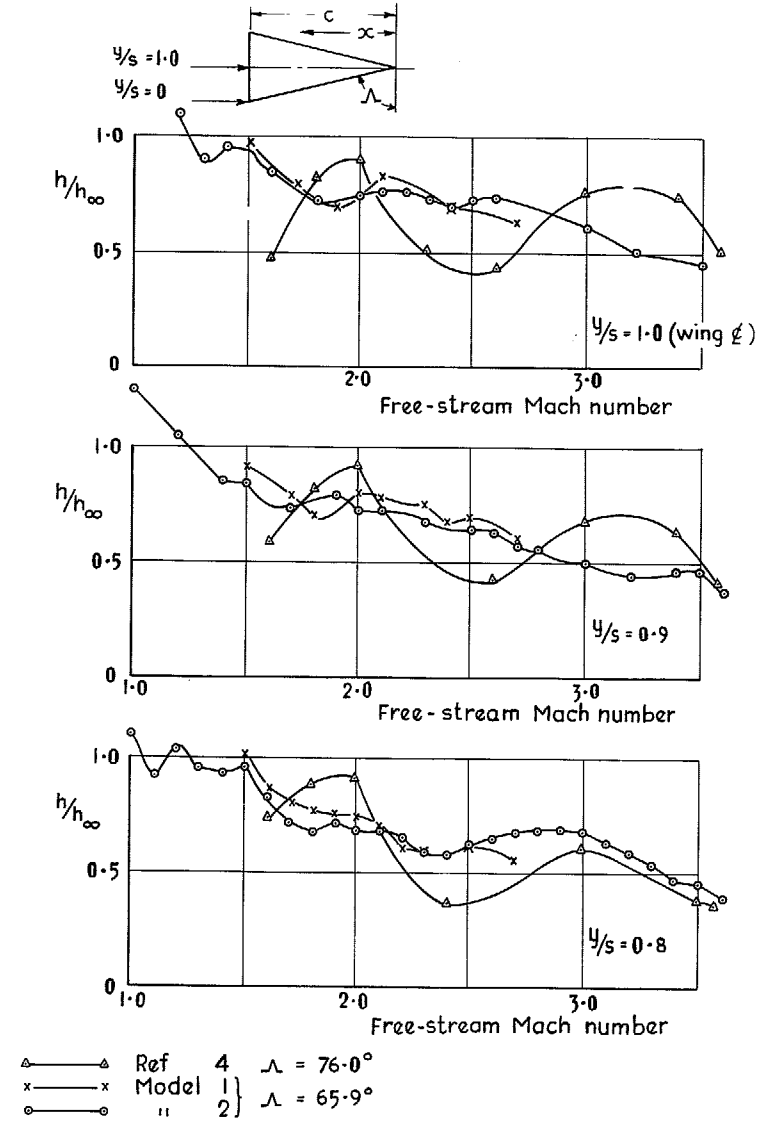

FIG. 14. Variation of heat transfer at spanwise stations with Mach number ($x/c = 0{\cdot}875$).

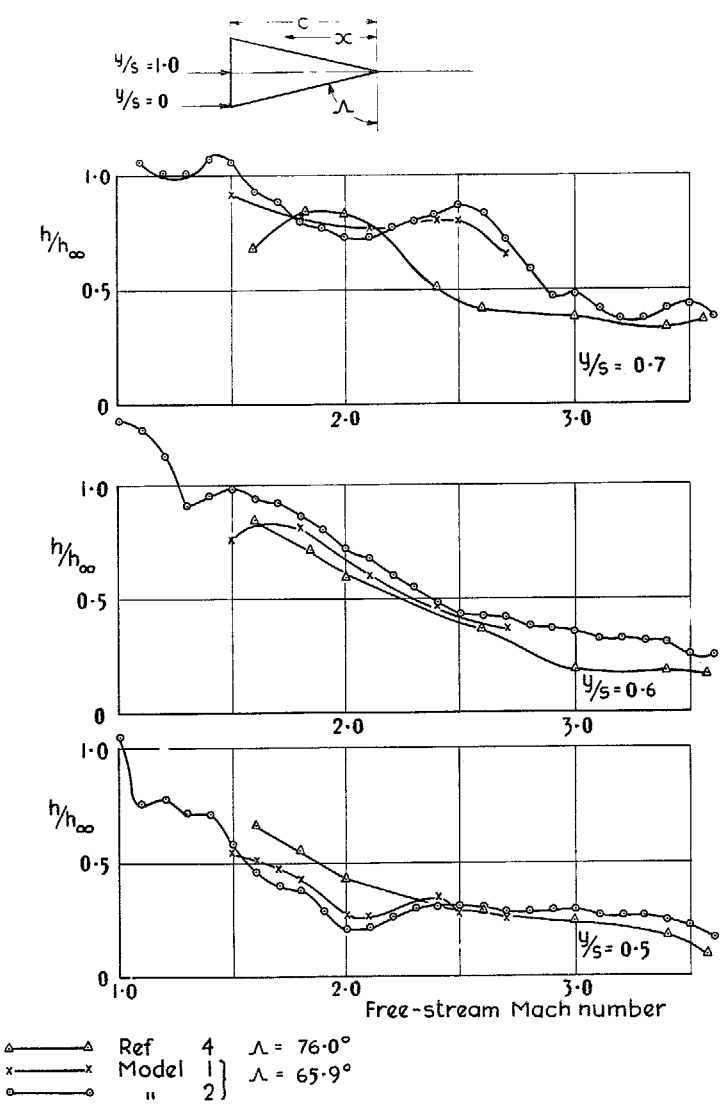

FIG. 14 *contd.* Variation of heat transfer at spanwise stations with Mach number ($x/c = 0{\cdot}875$).

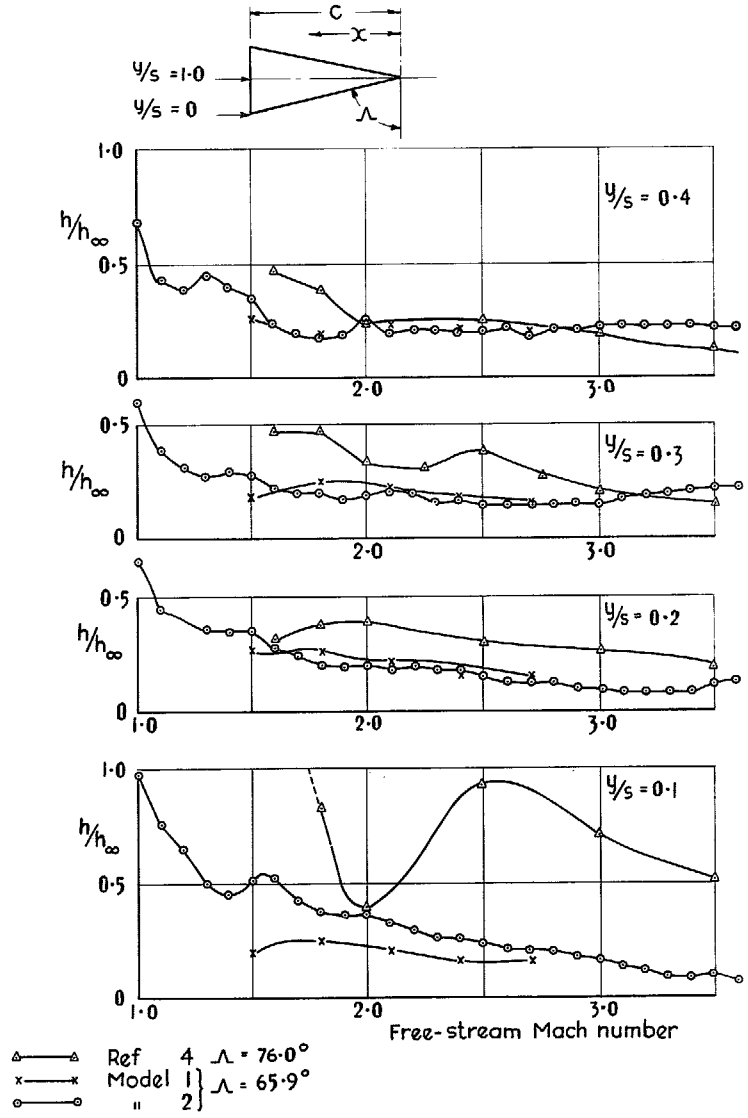

FIG. 14 *concld.* Variation of heat transfer at spanwise stations with Mach number ($x/c = 0{\cdot}875$).

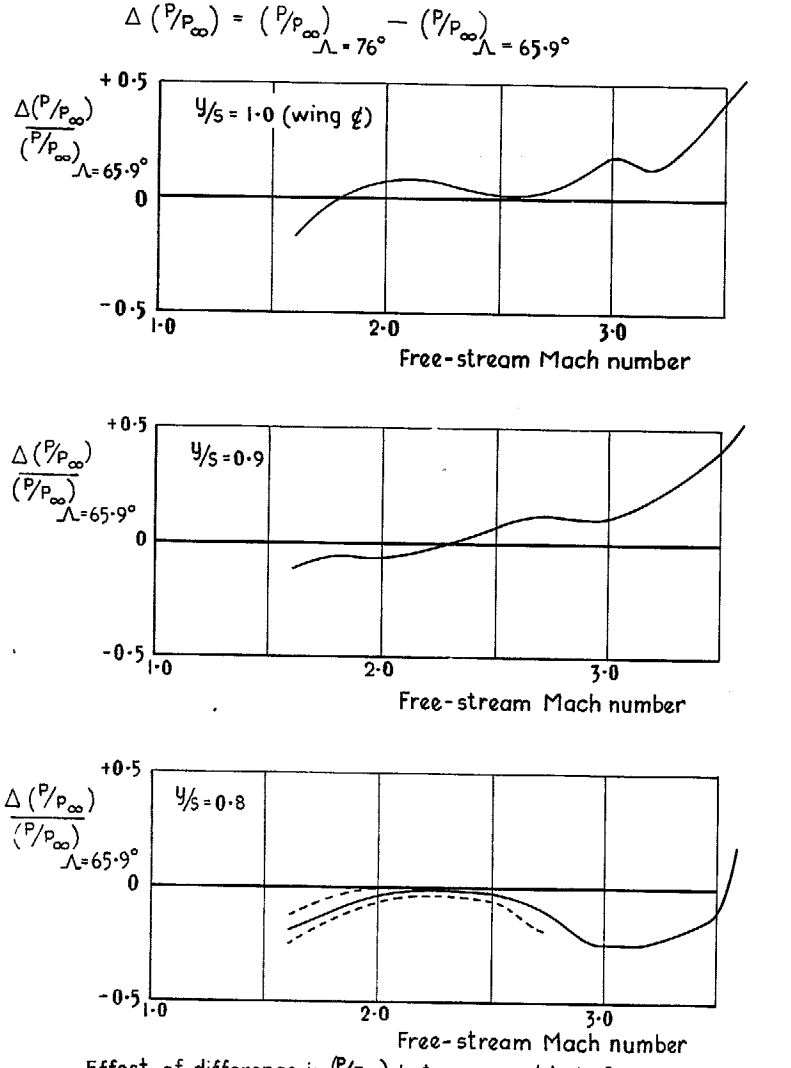

FIG. 15. Variation with Mach number at spanwise stations of the pressure increment resulting from a change in sweepback from $\Lambda = 65{\cdot}9°$ to 76°.

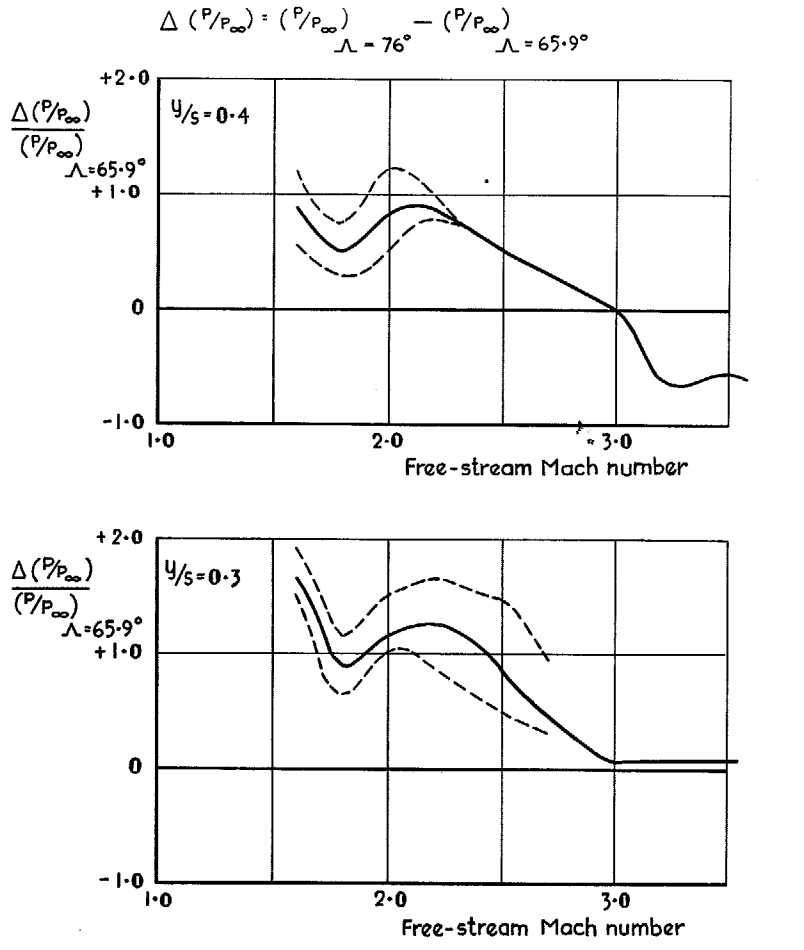

FIG. 15 *contd.* Variation with Mach number at spanwise stations of the pressure increment resulting from a change in sweepback from $\Lambda = 65{\cdot}9°$ to 76°.

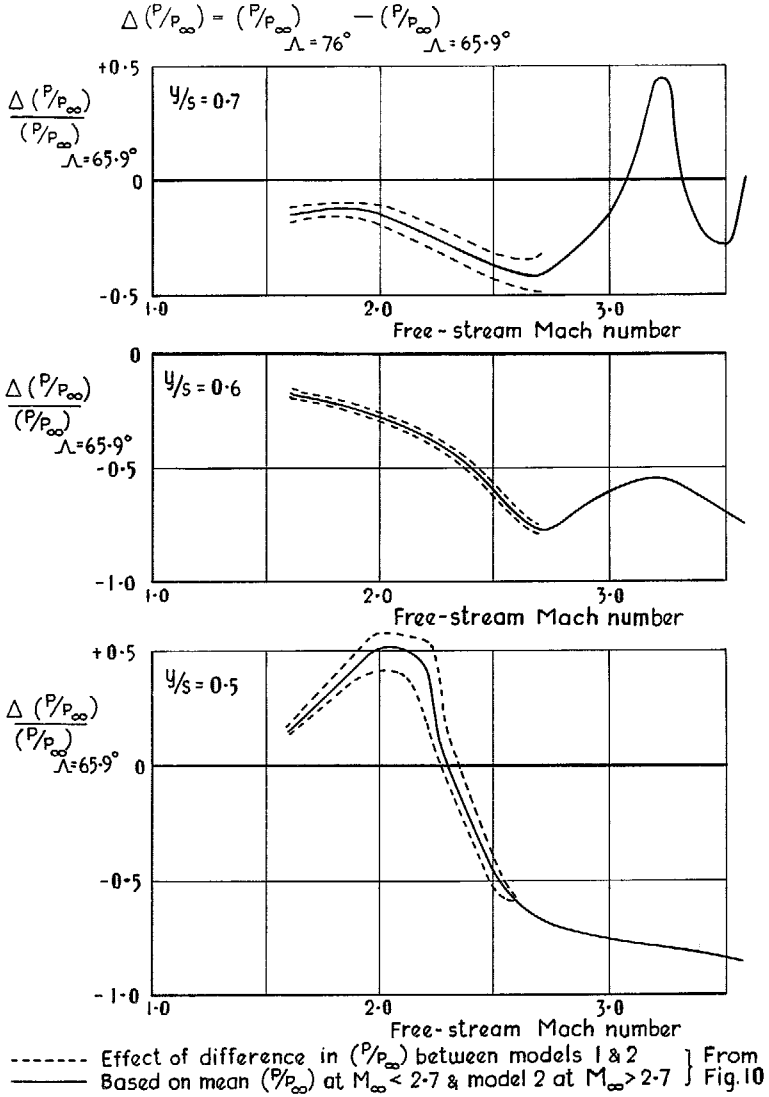

Fig.15 contd Variation with Mach number at spanwise stations of the pressure increment resulting from a change in sweepback from Λ = 65·9° to 76°

FIG. 15 *contd.* Variation with Mach number at spanwise stations of the pressure increment resulting from a change in sweepback from $\Lambda = 65{\cdot}9°$ to 76°.

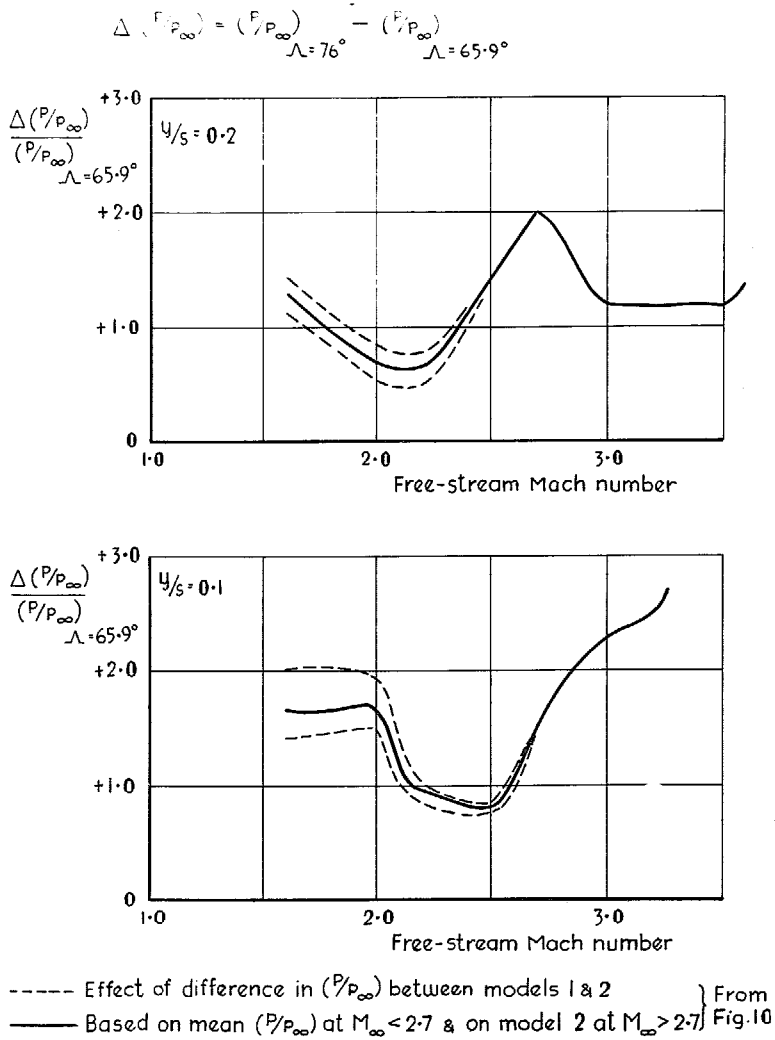

FIG. 15 *concld.* Variation with Mach number at spanwise stations of the pressure increment resulting from a change in sweepback from $\Lambda = 65{\cdot}9°$ to 76°.

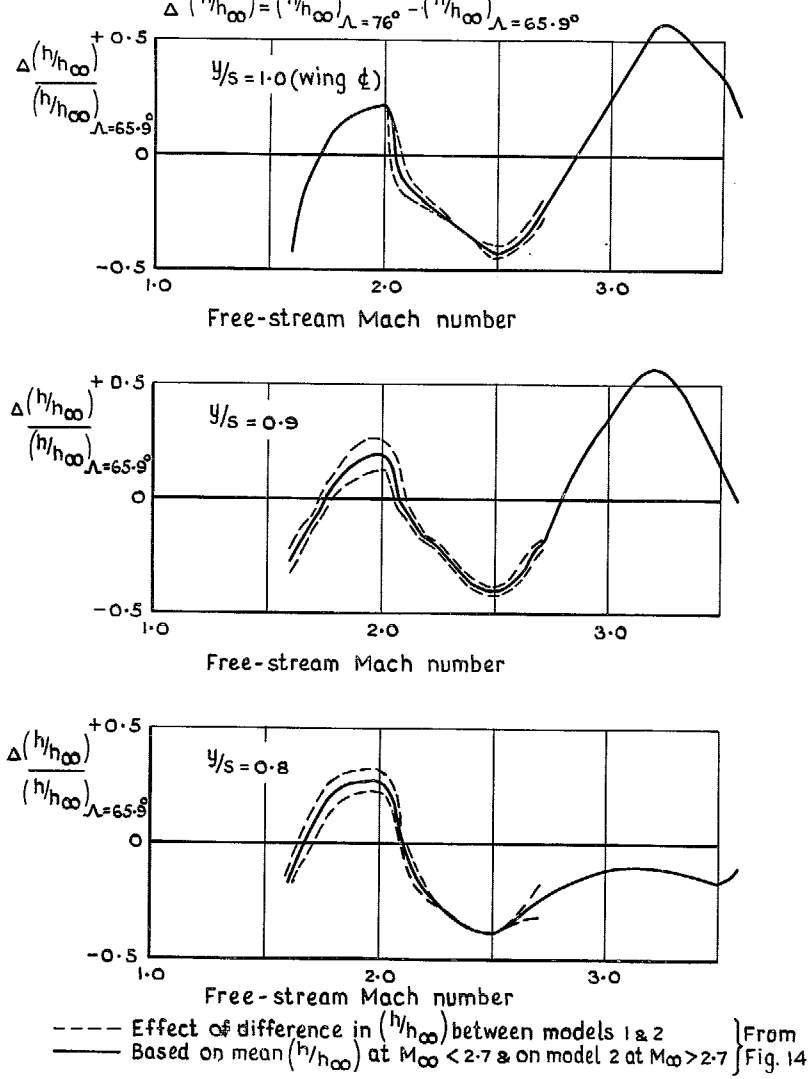

FIG. 16. Variation with Mach number at spanwise stations of the heat-transfer increment resulting from a change in sweepback from $\Lambda = 65·9°$ to 76°.

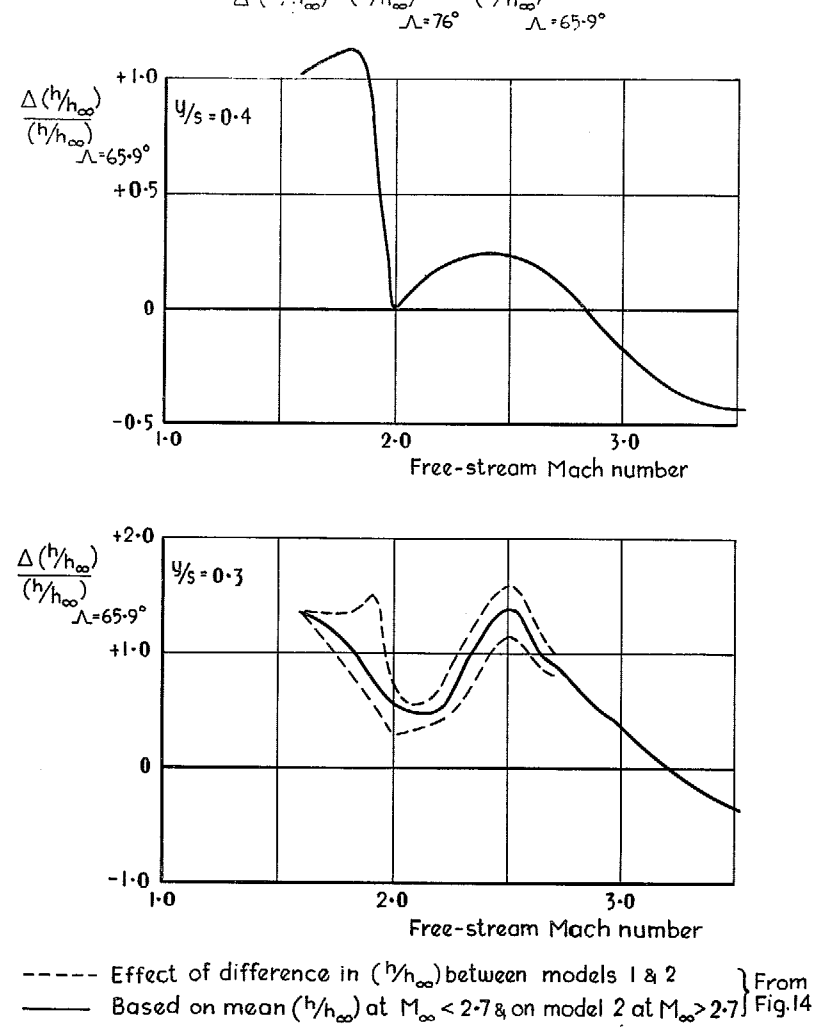

FIG. 16 *contd.* Variation with Mach number at spanwise stations of the heat-transfer increment resulting from a change in sweepback from $\Lambda = 65·9°$ to 76°.

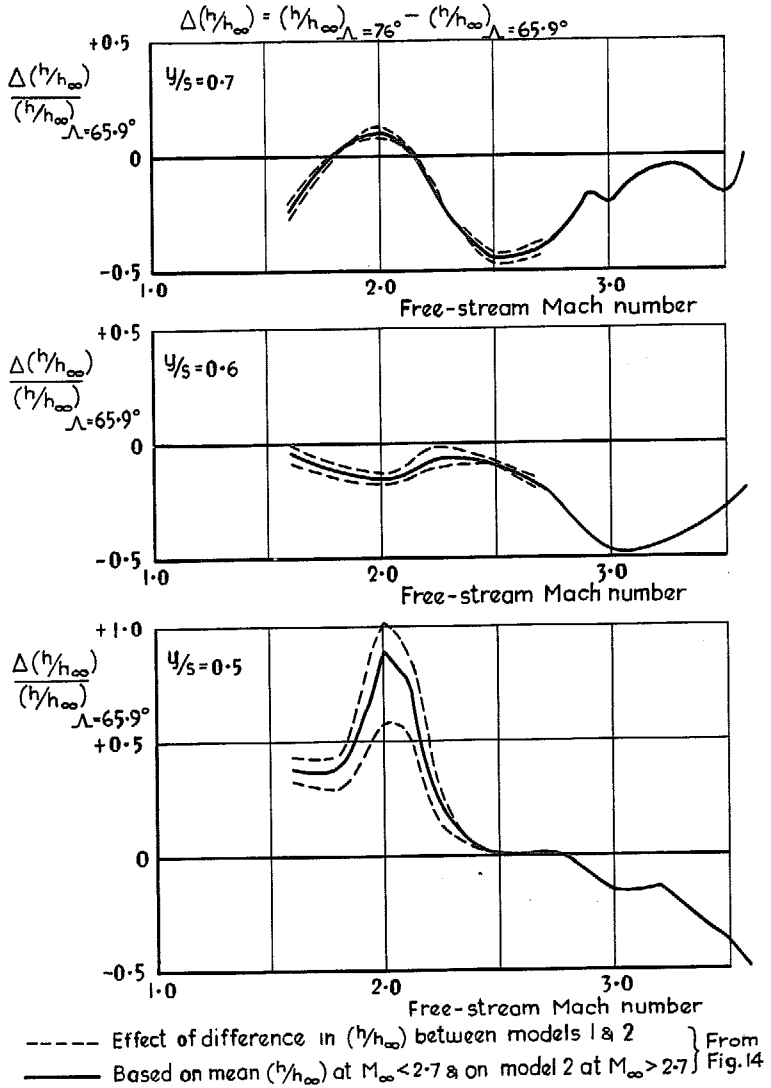

FIG. 16 *contd.* Variation with Mach number at spanwise stations of the heat-transfer increment resulting from a change in sweepback from $\Lambda = 65·9°$ to 76°.

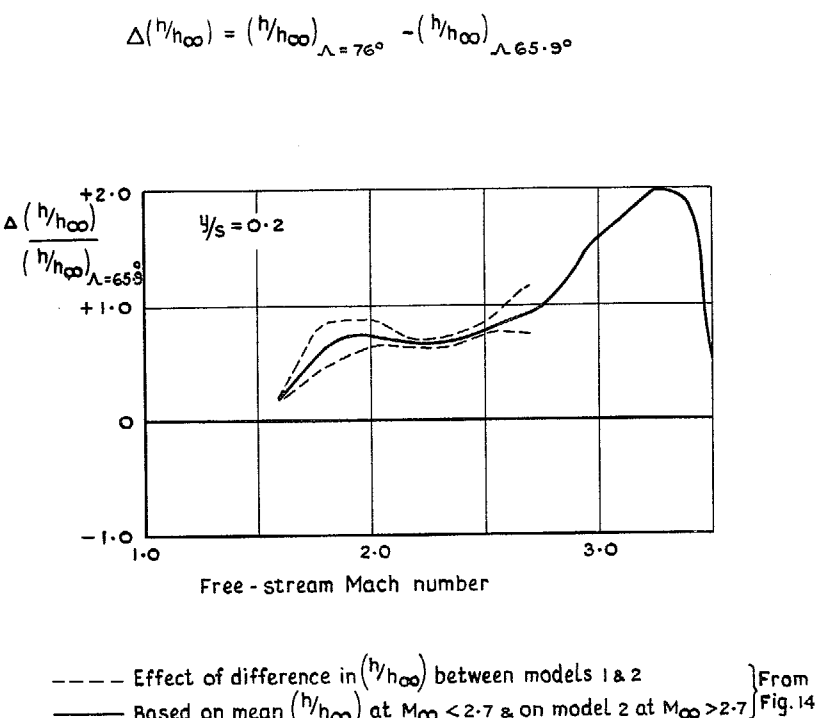

FIG. 16 *concld.* Variation with Mach number at spanwise stations of the heat-transfer increment resulting from a change in sweepback from $\Lambda = 65·9°$ to 76°.

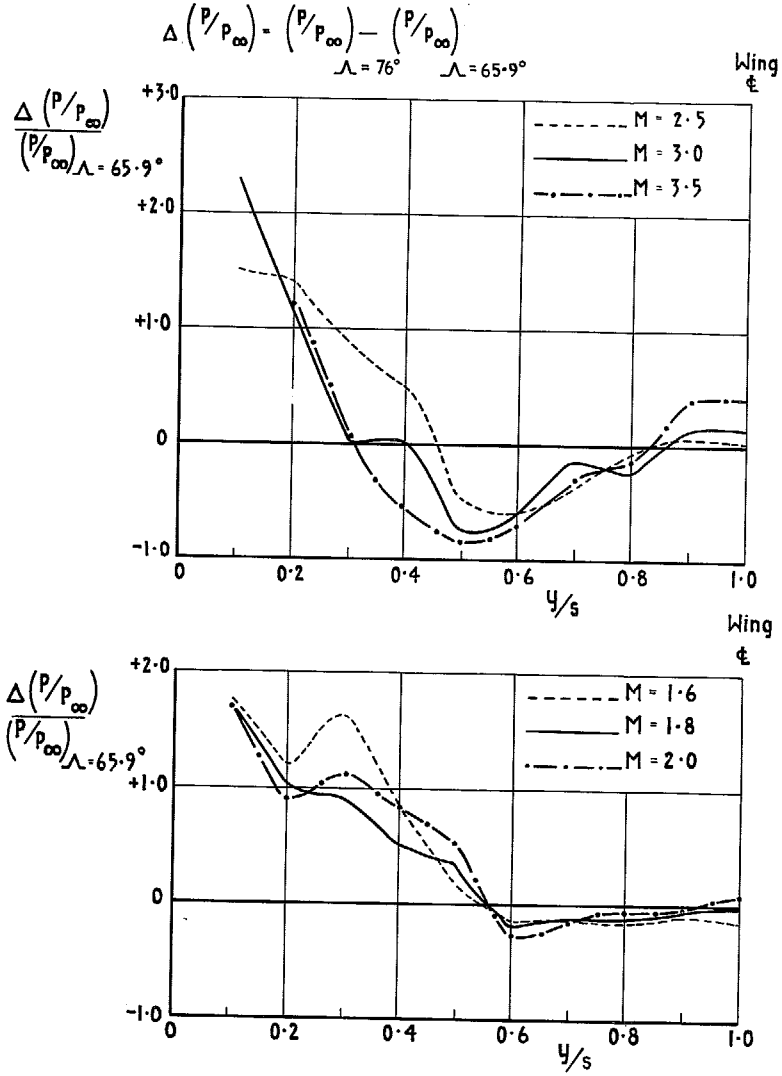

FIG. 17. Spanwise distribution at various Mach numbers of the pressure increment resulting from a change in sweepback from $\Lambda = 65{\cdot}9°$ to 76° (based on mean curves and Model 2 of fig. 15).

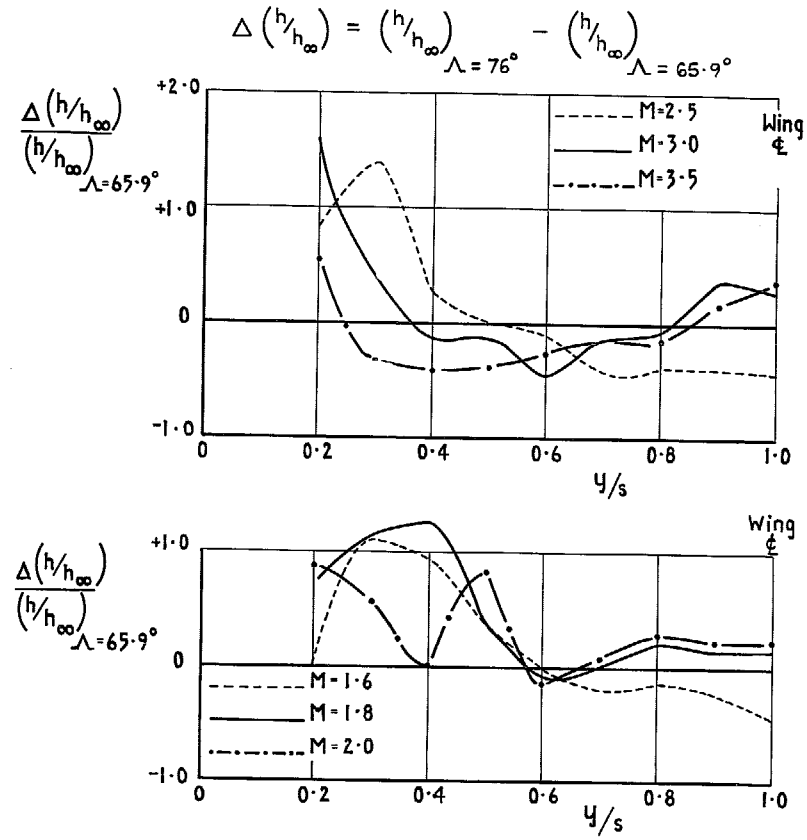

FIG. 18. Spanwise distribution at various Mach numbers of the heat-transfer increment resulting from a change in sweepback from $\Lambda = 65{\cdot}9°$ to 76° based on mean curves and Model 2 of fig. 15).

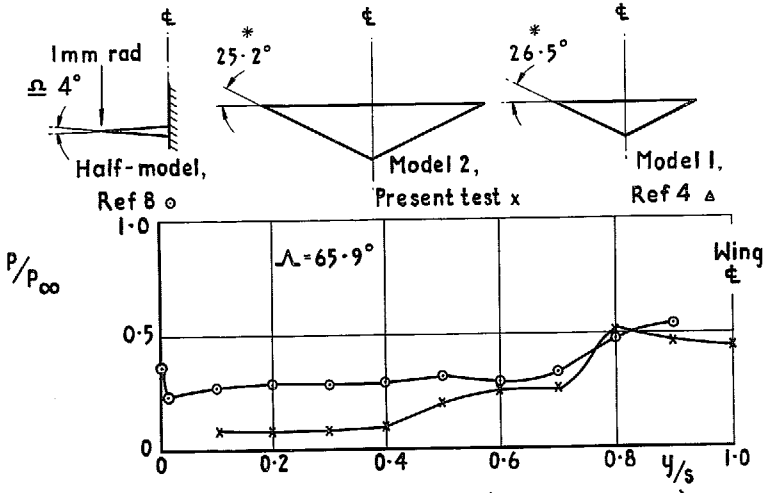

⊙ Thomann, ref 8, $\Lambda = 65{\cdot}9°$, $\alpha = 14{\cdot}5°$, Re (based on ℄ chord) $= 1{\cdot}3 \times 10^6$

x Model 2, present test, $\Lambda = 65{\cdot}9°$, $\alpha = 14{\cdot}0°$, Re (based on ℄ chord) $= 19{\cdot}0 \times 10^6$

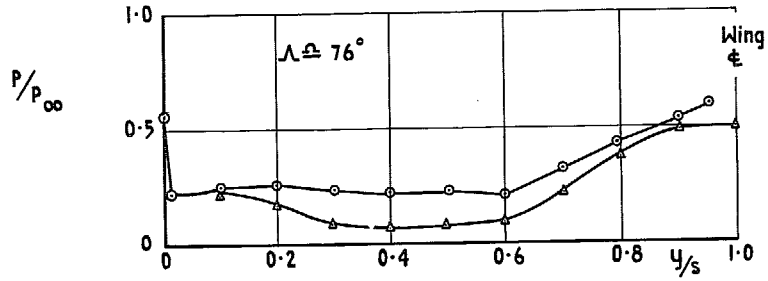

⊙ Thomann, ref 8, $\Lambda = 76{\cdot}0°$, $\alpha = 14{\cdot}5°$, Re (based on ℄ chord) $= 2{\cdot}0 \times 10^6$

△ Model 1, ref 4, $\Lambda = 76{\cdot}0°$, $\alpha = 14{\cdot}0°$, Re (based on ℄ chord) $= 20{\cdot}0 \times 10^6$

* Leading edge angle normal to leading edge was 27·3° for both models

FIG. 19. Comparison of the spanwise pressure distribution on the lee surface of Thomann's half-model (Ref. 8) with that on model 1 (Ref. 4) and on Model 2 (present test) at $M_\infty = 3{\cdot}0$.

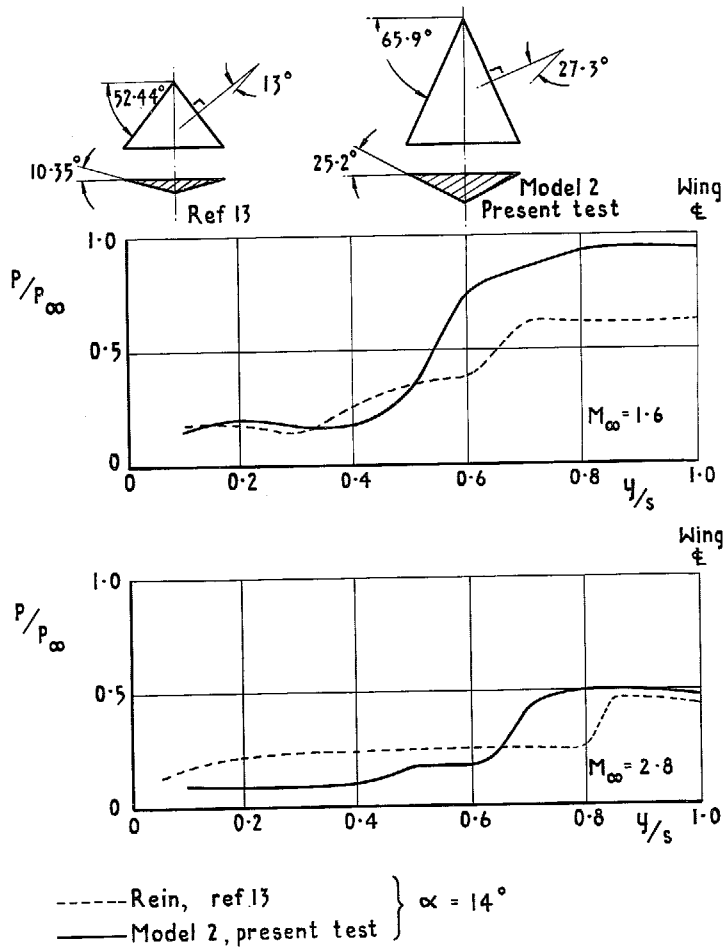

FIG. 20. Comparison of the spanwise pressure distribution on the flat lee surface of Rein's model (Ref. 13) with that on Model 2 (present test).

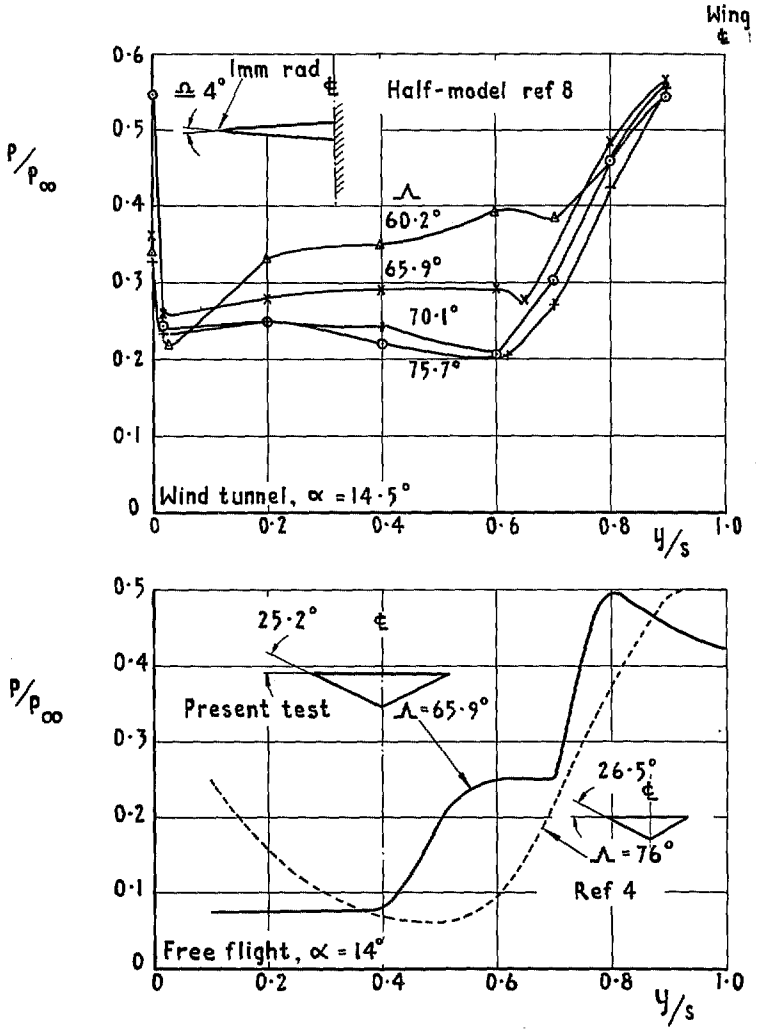

FIG. 21. Effect of sweepback on spanwise pressure distribution—wind-tunnel and free-flight tests at $M_\infty = 3{\cdot}0$.

Printed in Wales for Her Majesty's Stationery Office by Allens Printers (Wales) Limited

Dd 146916 K5

Published by
HER MAJESTY'S STATIONERY OFFICE

To be purchased from
49 High Holborn, London WC1
13a Castle Street, Edinburgh EH2 3AR
109 St Mary Street, Cardiff CF1 1JW
Brazennose Street, Manchester M60 8AS
50 Fairfax Street, Bristol BS1 3DE
258 Broad Street, Birmingham 1
7 Linenhall Street, Belfast BT2 8AY
or through any bookseller

R. & M. No. 3625
SBN 11 470325 6